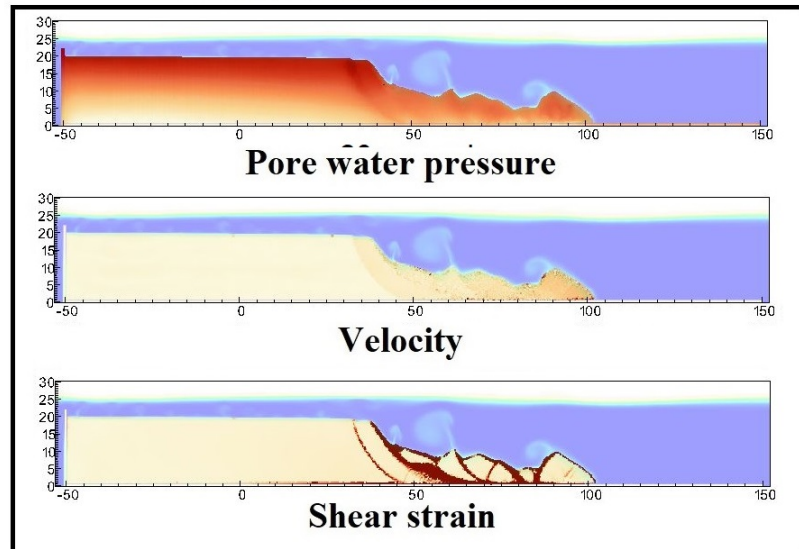


- 1 Graphical Abstract
- 2 MPMICE: A hybrid MPM-CFD model for simulating coupled problems in porous media. Application to earthquake-induced submarine landslides
- 3 Quoc Anh Tran, Gustav Grimstad, Seyed Ali Ghoreishian Amiri



**Application to earthquake-induced submarine landslide**

<sub>6</sub> Highlights

<sub>7</sub> **MPMICE: A hybrid MPM-CFD model for simulating coupled prob-**  
<sub>8</sub> **lems in porous media. Application to earthquake-induced subma-**  
<sub>9</sub> **rine landslides**

<sub>10</sub> Quoc Anh Tran, Gustav Grimstad, Seyed Ali Ghoreishian Amiri

- <sub>11</sub> • MPMICE is introduced for multiphase flow in porous media.
- <sub>12</sub> • Material Point method allows to model large deformation of non-isothermal
- <sub>13</sub> porous media.
- <sub>14</sub> • ICE (compressible multi-material CFD formulation) allows stabilizing
- <sub>15</sub> pore water pressure and turbulent flow.
- <sub>16</sub> • MPMICE is validated and apply to simulate the earthquake-induced
- <sub>17</sub> submarine landslide.

<sup>18</sup> MPMICE: A hybrid MPM-CFD model for simulating  
<sup>19</sup> coupled problems in porous media. Application to  
<sup>20</sup> earthquake-induced submarine landslides

<sup>21</sup> Quoc Anh Tran<sup>a,b</sup>, Gustav Grimstad<sup>a</sup>, Seyed Ali Ghoreishian Amiri<sup>a</sup>

<sup>a</sup>*Norwegian University of Science and Technology, , Trondheim, 7034, Norway*

<sup>b</sup>*quoc.a.tran@ntnu.no*

---

<sup>22</sup> **Abstract**

<sup>23</sup> In this paper, we describe a soil-fluid-structure interaction model that com-  
<sup>24</sup> bines soil mechanics (saturated sediments), fluid mechanics (seawater or air),  
<sup>25</sup> and solid mechanics (structures). The formulation combines the Material  
<sup>26</sup> Point Method, which models large deformation of the porous media and the  
<sup>27</sup> structure, with the Implicit Continuous-fluid Eulerian, which models com-  
<sup>28</sup> plex fluid flows. We validate the model and simulate the whole process of  
<sup>29</sup> earthquake-induced submarine landslides. We show that this model captures  
<sup>30</sup> complex interactions between saturated sediment, seawater, and structure,  
<sup>31</sup> so we can use the model to estimate the impact of potential submarine land-  
<sup>32</sup> slides on offshore structures.

<sup>33</sup> *Keywords:*

<sup>34</sup> Material Point Method, MPMICE, submarine landslide.

---

35	<b>Contents</b>	
36	<b>Nomenclature</b>	4
37	<b>Introduction</b>	6
38	<b>Theory and formulation</b>	8
39	Assumptions . . . . .	9
40	Governing equations . . . . .	9
41	Constitutive soil model . . . . .	11
42	Turbulent model . . . . .	12
43	Frictional force for soil-structure interaction . . . . .	13
44	Momentum and Energy exchange model . . . . .	13
45	Solving momentum and energy exchange with an implicit solver	15
46	Equation of state for fluid phases . . . . .	16
47	<b>Numerical implementation</b>	17
48	Interpolation from Solid Particle to Grid . . . . .	18
49	Compute equation of state for fluid phase . . . . .	20
50	Compute cell face velocity . . . . .	20
51	Compute cell face temperature . . . . .	21
52	Compute fluid pressure (implicit scheme) . . . . .	22
53	Compute viscous shear stress term of the fluid phase . . . . .	22
54	Compute nodal internal temperature of the solid phase . . . . .	23
55	Compute and integrate acceleration of the solid phase . . . . .	23
56	Compute Lagrangian value (mass, momentum and energy) . . . . .	23
57	Compute Lagrangian specific volume of the fluid phase . . . . .	25
58	Compute advection term and advance in time . . . . .	25
59	Interpolate from cell to node of the solid phase . . . . .	26
60	Update the particle variables . . . . .	26
61	<b>Numerical examples</b>	27
62	Fluid Flow through isothermal porous media . . . . .	27
63	Isothermal consolidation . . . . .	28
64	Thermal induced cavity flow . . . . .	29
65	Underwater debris flow . . . . .	31
66	Validation of soil response to the seismic loading . . . . .	33
67	Earthquake-induced submarine landslides . . . . .	37

68	<b>Conclusions</b>	42
69	<b>Acknowledgements</b>	43
70	<b>Appendix: Equation derivation</b>	43
71	Evolution of porosity . . . . .	43
72	Momentum conservation . . . . .	44
73	Energy conservation . . . . .	45
74	Advanced Fluid Pressure . . . . .	46
75	Momentum and Energy exchange with an implicit solver . . . . .	47

<sup>76</sup> **Nomenclature**

**General variables**

<u>Variable</u>	<u>Dimensions</u>	<u>Description</u>
$V$	$[L^3]$	Representative volume
$n$		Porosity
$\sigma$	$[ML^{-1}t^{-2}]$	Total stress tensor
$\Delta t$	$[t]$	Time increment
$\mathbf{b}$	$[ML^1t^{-2}]$	Body force
$c_v$	$[L^2t^{-2}T^{-1}]$	Constant volume specific heat
$f_d$	$[MLt^{-2}]$	Drag forces in momentum exchange term
$f^{int}$	$[MLt^{-2}]$	Internal forces
$f^{ext}$	$[MLt^{-2}]$	External forces
$q_{fs}$	$[MLt^{-2}]$	Heat exchange term
$S$		Weighting function
$\nabla S$		Gradient of weighting function

<sup>77</sup>

**Solid phase**

<u>Variable</u>	<u>Dimensions</u>	<u>Description</u>
$m_s$	$[M]$	Solid mass
$\rho_s$	$[ML^{-3}]$	Solid density
$\phi_s$		Solid volume fraction
$\bar{\rho}_s$	$[ML^{-3}]$	Bulk Solid density
$\mathbf{x}_s$	$[L]$	Solid Position vector
$\mathbf{U}_s$	$[Lt^{-1}]$	Solid Velocity vector
$\mathbf{a}_s$	$[Lt^{-2}]$	Solid Acceleration vector
$\sigma'$	$[ML^{-1}t^{-2}]$	Effective Stress tensor
$\epsilon$		Strain tensor
$e_s$	$[L^2t^{-2}]$	Solid Internal energy per unit mass
$T_s$	$[T]$	Solid Temperature
$\mathbf{F}_s$		Solid Deformation gradient
$V_s$	$[L^3]$	Solid Volume

**Fluid phase**

<u>Variable</u>	<u>Dimensions</u>	<u>Description</u>
$m_f$	[M]	Fluid mass
$\rho_f$	[ML <sup>-3</sup> ]	Fluid density
$\phi_f$		Fluid volume fraction
$\bar{\rho}_f$	[ML <sup>-3</sup> ]	Bulk Fluid density
$\mathbf{U}_f$	[Lt <sup>-1</sup> ]	Fluid Velocity vector
$\boldsymbol{\sigma}_f$	[ML <sup>-1</sup> t <sup>-2</sup> ]	Fluid stress tensor
$p_f$	[ML <sup>-1</sup> t <sup>-2</sup> ]	Fluid isotropic pressure
$\boldsymbol{\tau}_f$	[ML <sup>-1</sup> t <sup>-2</sup> ]	Fluid shear stress tensor
$e_f$	[L <sup>2</sup> t <sup>-2</sup> ]	Fluid Internal energy per unit mass
$T_f$	[T]	Fluid Temperature
$v_f$	[L <sup>3</sup> /M]	Fluid Specific volume $\frac{1}{\rho_f}$
$\alpha_f$	[1/T]	Thermal expansion
$\mu$	[ML <sup>-1</sup> t <sup>-1</sup> ]	Fluid viscosity
$V_f$	[L <sup>3</sup> ]	Fluid Volume

**Superscript**

<u>Variable</u>	<u>Dimensions</u>	<u>Description</u>
$n$		Current time step
$L$		Lagrangian values
$n + 1$		Next time step

**Subscript**

$c$	Cell-centered quantity
$p$	Particle quantity
$i$	Node quantity
$FC$	Cell face quantity
$L, R$	Left and Right cell faces

79 **Introduction**

80 Many geological natural processes and their interactions with man-made  
81 structures are influenced by soil-fluid-structure interactions. The prediction  
82 of these processes requires a tool that can capture complex interactions  
83 between soil, fluid, and structure, such as the process of submarine land-  
84 slides. Indeed, The offshore infrastructure as well as coastal communities  
85 may be vulnerable to submarine landslides. Submarine landslides contain  
86 three stages: triggering, failure, and post-failure. Erosion or earthquakes can  
87 trigger slope failures in the first stage. Following the failure, sediments move  
88 quickly after the post-failure stage. In other words, solid-like sediments will  
89 behave like a fluid after failure. This transition, where the sediment trans-  
90 forms into fluid-like debris and then re-establishes a porous medium, poses  
91 a challenging task for simulating submarine landslides.

92  
93 Due to this transition, submarine landslides can be modeled using ei-  
94 ther the Eulerian framework or the Lagrangian framework. The Eulerian  
95 framework involves calculation of material response at specific time-space  
96 points. For instance, methods within Computational fluid Dynamics, exam-  
97 ple using Finite Volume Methods (FVM) are employed to simulate subma-  
98 rine landslides [1, 2, 3, 4] by solving governing equations in a full-Eulerian  
99 framework. While FVM is capable of handling complex flows, such as tur-  
100 bulent flows, it falls short in accounting for the triggering mechanisms of  
101 submarine landslides. This is due to the challenge of incorporating 'con-  
102 stitutive laws' of sediment materials within the Eulerian framework. This  
103 is particularly significant because converting material time derivatives into  
104 fixed space derivatives involves arduous mathematical tasks, especially for  
105 soil materials that rely on nonlinear tensor operations and history-dependent  
106 state/internal variables. In contrast, the Lagrangian framework, including  
107 various particle-based methods, provides a solution to this problem. In the  
108 Lagrangian framework, material "particles" are tracked individually through  
109 space, and material properties and internal variables are determined at and  
110 follows these particles. These methods have been extensively used to simulate  
111 landslides, like Material Point Method (MPM) [5], Smooth Particle Hydro  
112 Dynamics [6], Particle Finite Element Method [7], or Coupled Eulerian La-  
113 grangian Method [8]. For simplicity, these previous simulations have adopted  
114 a total stress analysis, neglecting the pore pressure development which is a  
115 key factor triggering slope failures.

116 Recent developments in particle-based Lagrangian methods model the cou-  
 117 pling of fluid flows in porous media by sets of Lagrangian particles. For the  
 118 MPM family, it is the double-point MPM ([9, 10, 11]) where fluid particles  
 119 and solid particles are overlapped in a single computational grid. Even if  
 120 fluid flows are considered, particle-based methods have numerical instability  
 121 in modeling the fluid flow, which requires additional numerical treatments  
 122 such as the B-bar method [9], null-space filter [12], or least square approxima-  
 123 tion [13, 14]. For complex and turbulent fluid flows like submarine landslides,  
 124 Eulerian methods like FVM/CFD are preferred when turbulence occurs at  
 125 fine resolutions due to their computational efficiency. Therefore, it could  
 126 be ideal to combine the CFD with particle-based methods. More than 50  
 127 particle-based methods have been developed to solve large deformations of  
 128 solids over the last two decades [15], but the MPM appears to be the best  
 129 candidate for coupling with the CFD. Because MPM incorporates a station-  
 130 ary mesh during computation, just like CFD. As such, both MPM and CFD  
 131 can be coupled naturally in a unified computational mesh.

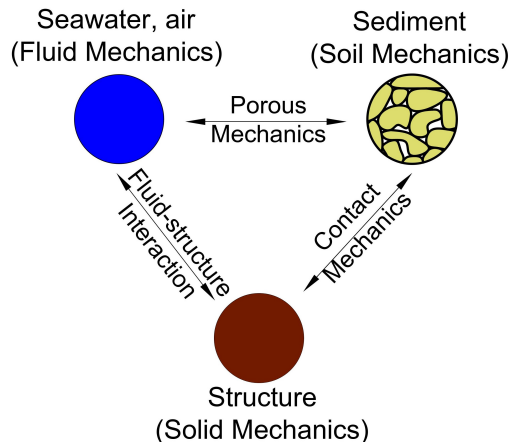


*Figure 1: Interaction between soil-fluid-structure*

132  
 133 A numerical method for simulating soil-fluid-structure interaction (Fig-  
 134 ure 1) involving large deformations, is presented in this work in order to  
 135 simulate the interaction between sediment (soil), seawater (fluid) and off-  
 136 shore structures (structure) namely MPMICE (Figure 2). In the MPMICE,  
 137 the Material Point Method (MPM) is coupled with the Implicit Continuous  
 138 Eulerian (ICE) [16]. The MPM method is a particle method that allows the

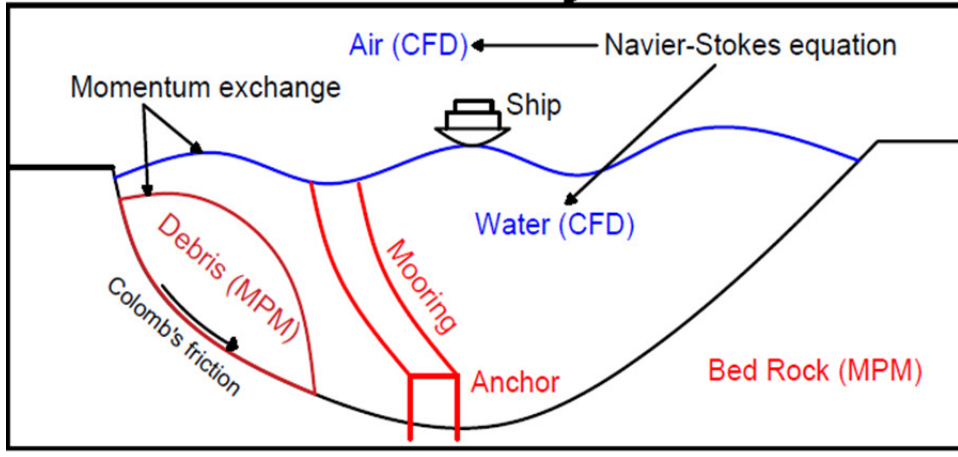


*Figure 2: Coupling of soil-water-structure interaction using MPMICE*

porous soil to undergo arbitrary distortions. The ICE method, on the other hand, is a conservative finite volume technique with all state variables located at the cell center (temperature, velocity, mass, pressure). The ICE method offers certain advantages in comparison to conventional FVM in the realm of flow computation encompassing all velocity ranges. An initial technical report [17] at Los Alamos National Laboratory provided the theoretical and algorithmic foundation for the MPMICE, followed by the MPMICE development and implementation in the high-performance Uintah computational framework for simulating fluid-structure interactions [18]. This paper primarily contributes further to the development of the MPMICE for analyzing the **soil**-fluid-structure interaction, since sediment should be considered as a porous media (soil) and not as a solid to capture the evolution of the pore water pressure. Baumgarten et al. [19] made the first attempt at coupling the FVM with the MPM for the simulation of soil-fluid interaction by using an explicit time integration for the single-phase flow. In contrast to the mentioned work, we use implicit time integration for the multi phase flows.

### 155      Theory and formulation

This section lay out the theoretical framework for the MPMICE model. We use the common notation of the continuum mechanics with vector and tensor denoted simply by using bold font and scalar denoted by using normal font. The notation are shown in Nomenclature.

160 *Assumptions*

161 The following assumptions are made for the MPMICE model.

- 162 1. Solid phases (MPM) are described in a Lagrangian formulation while  
163 fluid phases (ICE) are described in an Eulerian formulation in the  
164 framework of continuum mechanics and mixture theory.  
165 2. Solid grains are incompressible while the fluid phases are compressible.  
166 3. There is no mass exchange between solid and fluid phases.  
167 4. Terzaghi's effective stress is valid.

168 *Governing equations*

169 A representative element volume  $\Omega$  is decomposed by two domains: solid  
170 domains  $\Omega_s$  and fluid domains  $\Omega_f$ . Then, all domains are homogenized  
171 into two overlapping continua. Considering the volume fraction of solid  
172  $\phi_s = \Omega_s/\Omega$  and fluid  $\phi_f = \Omega_f/\Omega$  with the true (or Eulerian) porosity  
173  $n = \sum \phi_f$  of the representative element volume, the average density of solid  
174 and fluid phases are defined as:

175

$$\bar{\rho}_s = \phi_s \rho_s, \quad \bar{\rho}_f = \phi_f \rho_f \quad (1)$$

176 The mass of solid and fluid phases are:

177

$$m_s = \int_{\Omega_s} \rho_s dV = \bar{\rho}_s V, \quad m_f = \int_{\Omega_f} \rho_f dV = \bar{\rho}_f V \quad (2)$$

178 Reviewing the Terzaghi's effective stress concept for the saturated porous  
179 media, the total stress  $\boldsymbol{\sigma}$  is calculated by:

180

$$\boldsymbol{\sigma} = \boldsymbol{\sigma}' - p_f \mathbf{I} \quad (3)$$

181 The balance equations are derived based on the mixture theory. The rep-  
182 resentative thermodynamic state of the fluid phases are given by the vector  
183  $[m_f, \mathbf{U}_f, e_f, T_f, v_f]$  which are mass, velocity, internal energy, temperature,  
184 specific volume. The representative state of the solid phases are given by the  
185 vector  $[m_s, \mathbf{U}_s, e_s, T_s, \boldsymbol{\sigma}', p_f]$  which are mass, velocity, internal energy, temper-  
186 ature, effective stress and pore water pressure. The derivation is presented  
187 in detail in the Appendix.

188

---

189 **Mass Conservation**

190 The mass balance equations for both fluid (e.g., water, air) and solid phases

191 are:

192

$$\frac{1}{V} \frac{\partial m_f}{\partial t} + \nabla \cdot (m_f \mathbf{U}_f) = 0, \frac{1}{V} \frac{D_s m_s}{Dt} = 0 \quad (4)$$

193 Solving the mass balance equation of the solid phase leads to:

$$\frac{D_s n}{Dt} = \phi_s \nabla \cdot \mathbf{U}_s \quad (5)$$

194

---

### 195 Momentum Conservation

196 The momentum balance equations for each fluid phases (e.g., water, air) are:

$$\frac{1}{V} \left[ \frac{\partial(m_f \mathbf{U}_f)}{\partial t} + \nabla \cdot (m_f \mathbf{U}_f \mathbf{U}_f) \right] = -\phi_f \nabla p_f + \nabla \cdot \boldsymbol{\tau}_f + \bar{\rho}_f \mathbf{b} + \sum \mathbf{f}_d \quad (6)$$

197 The momentum balance equations for each solid phases are:

$$\frac{1}{V} \frac{D_s(m_s \mathbf{U}_s)}{Dt} = \nabla \cdot (\boldsymbol{\sigma}') - \phi_s \nabla p_f + \bar{\rho}_s \mathbf{b} + \sum \mathbf{f}_{fric} - \sum \mathbf{f}_d \quad (7)$$

198

---

### 199 Energy Conservation

200 The internal energy balance equations for each fluid phases (e.g., water, air)  
201 are:

$$\frac{1}{V} \left[ \frac{\partial(m_f e_f)}{\partial t} + \nabla \cdot (m_f e_f \mathbf{U}_f) \right] = -\bar{\rho}_f p_f \frac{D_f v_f}{Dt} + \boldsymbol{\tau}_f : \nabla \mathbf{U}_f + \nabla \cdot \mathbf{q}_f + \sum q_{sf} \quad (8)$$

202 The internal energy balance equations for each solid phases are:

$$\frac{m_s}{V} c_v \frac{D_s(T_s)}{Dt} = \boldsymbol{\sigma}' : \frac{D_s(\boldsymbol{\epsilon}_s^p)}{Dt} + \nabla \cdot \mathbf{q}_s - \sum q_{sf} \quad (9)$$

203 where  $c_v$  is the specific heat at constant volume of the solid materials.

204

---

205 Closing the systems of equations, the following additional models are needed:

206 (1) A constitutive equation to describe the stress - strain behaviour of solid  
207 phase (computing effective stress  $\boldsymbol{\sigma}'$ ).

208 (2) Optional turbulent model to compute the viscous shear stress  $\boldsymbol{\tau}_f$ .

209 (3) Frictional forces  $\mathbf{f}_{fric}$  for the contact for soil-structure interaction be-  
210 tween solid/porous materials with the friction coefficient  $\mu_{fric}$ .

- 211 (4) Exchange momentum models (computing drag force  $\mathbf{f}_d$ ) for interaction  
 212 between materials.  
 213 (5) Energy exchange models (computing temperature exchange term  $q_{sf}$ ) for  
 214 interaction between materials.  
 215 (6) An equation of state to establish relations between thermodynamics vari-  
 216 ables of each fluid materials  $[P_f, \bar{\rho}_f, v_f, T_f, e_f]$ .  
 217 (7) Thermal conduction model to compute thermal flux of solid phase  $\mathbf{q}_s$  and  
 218 liquid phase  $\mathbf{q}_s$ .
- 219 Four thermodynamic relations for the equation of states are:

$$\begin{aligned} e_f &= e_f(T_f, v_f) \\ P_f &= P_f(T_f, v_f) \\ \phi_f &= v_f \bar{\rho}_f \\ 0 &= n - \sum_{f=1}^{N_f} v_f \bar{\rho}_f \end{aligned} \tag{10}$$

220 *Constitutive soil model*

221 As a result of the explicit MPM formulation, we can derive the consti-  
 222 tutive law in the updated Lagrangian framework of "small strain - large  
 223 deformation". Therefore, the rotation of the particles (representative ele-  
 224 ment volume) is manipulated by rotating the Cauchy stress tensor. First,  
 225 the deformation gradient is decomposed into the polar rotation tensor  $\mathbf{R}_s^{n+1}$   
 226 and stretch tensor  $\mathbf{V}_s^{n+1}$  as:

$$\mathbf{F}_s^{n+1} = \mathbf{V}_s^{n+1} \mathbf{R}_s^{n+1} \tag{11}$$

227 Then, before calling the constitutive model, the stress and strain rate tensor  
 228 are rotated to the reference configuration as:

$$\boldsymbol{\sigma}'^{n*} = (\mathbf{R}_s^{n+1})^T \boldsymbol{\sigma}'^n \mathbf{R}_s^{n+1} \tag{12}$$

$$\delta\boldsymbol{\epsilon}^{n*} = (\mathbf{R}_s^{n+1})^T \delta\boldsymbol{\epsilon}^n \mathbf{R}_s^{n+1} \tag{13}$$

230 Using the constitutive model with the input tensors  $\boldsymbol{\sigma}'^{n*}, \delta\boldsymbol{\epsilon}^{n*}$  to compute  
 231 the Cauchy stress tensor at the advanced time step  $\boldsymbol{\sigma}'^{n+1*}$  then rotating it  
 232 back to current configuration as:

$$\boldsymbol{\sigma}'^{n+1} = \mathbf{R}_s^{n+1} \boldsymbol{\sigma}'^{n+1*} (\mathbf{R}_s^{n+1})^T \tag{14}$$

233 In this paper, we adopt the hyper-elastic Neo Hookean model for the structure  
 234 materials and additionally Mohr-Coulomb failure criteria for the soil (porous  
 235 media) materials. The Cauchy stress of the hyper-elastic Neo Hookean model  
 236 can be written as:

$$\boldsymbol{\sigma}' = \frac{\lambda \ln(J)}{J} + \frac{\mu}{J} (\mathbf{F}\mathbf{F}^T - \mathbf{J}) \quad (15)$$

237 where  $\lambda$  and  $\mu$  are bulk and shear modulus ad  $J$  is the determinant of the  
 238 deformation gradient  $\mathbf{F}$ . And the yield function  $f$  and flow potentials  $g$  of  
 239 the Mohr-Coulomb can be written as:

$$\begin{aligned} f &= -\sigma'_1 + \sigma'_3 + 2c' \cos(\phi') + (\sigma'_1 + \sigma'_3) \sin(\phi') \\ g &= -\sigma'_1 + \sigma'_3 + 2c' \cos(\psi') + (\sigma'_1 + \sigma'_3) \sin(\psi') \end{aligned} \quad (16)$$

240 In the equations,  $c'$ ,  $\phi'$ , and  $\psi'$  represent the cohesion, friction angle, and  
 241 dilation angle, respectively.  $\sigma'_1$  and  $\sigma'_3$  denote the maximum and minimum  
 242 principal stresses, with the condition  $\sigma'_1 < \sigma'_3 < 0$ . It is important to note  
 243 that in our assumptions, stress is considered positive during extension, which  
 244 means the signs of the stresses in these equations are opposite to those in  
 245 standard Soil Mechanic's textbooks. The numerical implementation follows  
 246 the approach described in Clausen et al. [20].

#### 247 *Turbulent model*

248 The turbulent effect is modelled using a statistical approach namely large-  
 249 eddy simulation. In this approach, the micro-scale turbulent influence in the  
 250 dynamics of the macro-scale motion is computed through simple models like  
 251 Smagorinsky model [21]. In the Smagorinsky model, the residual stress tensor  
 252 is:

$$\tau_{ij} = 2\mu_{eff}(\bar{S}_{ij} - \frac{1}{3}\delta_{ij}\bar{S}_{kk}) + \frac{1}{3}\delta_{ij}\tau_{kk} \quad (17)$$

253 where the the strain rate tensor is given by:

$$\bar{S}_{ij} = \frac{1}{2}(\frac{\delta \bar{\mathbf{U}}_i}{\delta x_j} + \frac{\delta \bar{\mathbf{U}}_j}{\delta x_i}) \quad (18)$$

254 and the effective viscosity is sum of molecular viscosity and turbulent viscos-  
 255 ity  $\mu_{eff} = \mu + \mu_t$  in which the turbulent viscosity  $\mu_t$  is calculated by:

$$\mu_t = (C_s \Delta)^2 \sqrt{2\bar{S}_{ij}\bar{S}_{ij}} \quad (19)$$

256 where  $C_s$  is the Smagorinsky constant with the value of 0.1 and  $\Delta = \sqrt[3]{dxdydz}$   
 257 is the grid size that defines the subgrid length scale.

258 *Frictional force for soil-structure interaction*

259 MPMICE includes a contact law for the interaction between soil and  
260 structure using the first Coulomb friction contact for MPM presented by  
261 Bardenhagen et al. [22]. The magnitude of the friction force at the contact  
262 depends on the friction coefficient  $\mu_{fric}$  and the normal force  $\mathbf{f}_{norm}$  computed  
263 from the projection of the contact force in the normal direction.

$$\mathbf{f}_{fric} = \mu_{fric} \mathbf{f}_{norm} \quad (20)$$

264 The contact determines whether the soil is sliding or sticking to the structure  
265 by comparing the friction force with the sticking force  $\mathbf{f}_{stick}$  can be computed  
266 from the projection of the contact force in the tangent direction as:

$$\begin{aligned} & \text{if } \mathbf{f}_{fric} \geq \mathbf{f}_{stick} \text{ no sliding} \\ & \text{if } \mathbf{f}_{fric} < \mathbf{f}_{stick} \text{ sliding occurs} \end{aligned} \quad (21)$$

267 Frictional sliding between solid materials also generates dissipation and the  
268 work rate generated from the sliding can be calculated as:

$$\Delta W_{friction} = \mathbf{f}_{fric} d \quad (22)$$

269 where  $d$  is the sliding distance which can be computed based on the sliding  
270 velocity between two materials.

271 *Momentum and Energy exchange model*

272 Currently, the energy exchange coefficient  $H_{sf}$  is assumed to be constant  
273 for the sake of simplicity. Then the energy exchange can be written as:

$$q_{sf} = H_{sf} (T_f - T_s) \quad (23)$$

274 On the other hand, the drag force can be calculated as:

$$f_d = K(\mathbf{U}_s - \mathbf{U}_f) \quad (24)$$

275 For the momentum exchange between fluid flows and porous media, we as-  
276 sume that the drag force  $\mathbf{f}_d$  depends on the average grain size of the grains  
277  $D_p$ , the porosity  $n$ , the fluid viscosity  $\mu_f$ , and is proportional to the relative  
278 velocities of soil grains and fluid  $(\mathbf{U}_s - \mathbf{U}_f)$ . Based on recent investigation  
279 of CFD simulations of fluid flow around mono- and bi-disperse packing of

<sup>280</sup> spheres for  $0.1 < \phi_s < 0.6$  and  $Re < 1000$  [23]. The drag force is given by:

<sup>281</sup>

$$\mathbf{f}_d = \frac{18\phi_s(1-\phi_s)\mu_f}{D_p^2} F(\phi_s, Re)(\mathbf{U}_s - \mathbf{U}_f) \quad (25)$$

<sup>282</sup> where Reynolds number  $Re$  are computed as:

$$Re = \frac{n\rho_f D_p}{\mu_f} \|\mathbf{U}_s - \mathbf{U}_f\| \quad (26)$$

<sup>283</sup> The function  $F(\phi_s, Re)$  can be calculated as:

$$F(\phi_s, Re) = F(\phi_s, 0) + \frac{0.413Re}{24(1-\phi_s)^2} \left( \frac{(1-\phi_s)^{-1} + 3\phi_s(1-\phi_s) + 8.4Re^{-0.343}}{1 + 10^{3\phi_s} Re^{-(1+4\phi_s)/2}} \right) \quad (27)$$

<sup>284</sup> where the low Reynold coefficient  $F(\phi_s, Re \rightarrow 0)$  is:

$$F(\phi_s, 0) = \frac{10\phi_s}{(1-\phi_s)^2} + (1-\phi_s)^2(1 + 1.5\sqrt{\phi_s}) \quad (28)$$

<sup>285</sup> When validating the model with analytical solution, it requires to know the  
<sup>286</sup> hydraulic conductivity  $K$ . In such case, we convert the equation (25) to  
<sup>287</sup> Kozeny-Carman formula by assuming  $F(\phi_s, Re) = 10\phi_s/(1-\phi_s)^2$ , leading to

$$\mathbf{f}_d = \frac{180\phi_s^2\mu_f}{D_p^2(1-\phi_s)} (\mathbf{U}_s - \mathbf{U}_f) \quad (29)$$

<sup>288</sup> Then, the draging force following the Darcy law is given by:

$$\mathbf{f}_d = \frac{n^2\mu_f}{\kappa} (\mathbf{U}_s - \mathbf{U}_f) \quad (30)$$

<sup>289</sup> where  $\kappa$  being intrinsic permeability of soil which can be written as:

$$\kappa = \frac{K\mu_f}{\rho_f g} \quad (31)$$

<sup>290</sup> As such, the hydraulic conductivity will be expressed as:

$$K = \frac{D_p^2(1-\phi_s)^3}{180\phi_s^2\mu_f} \rho_f g \quad (32)$$

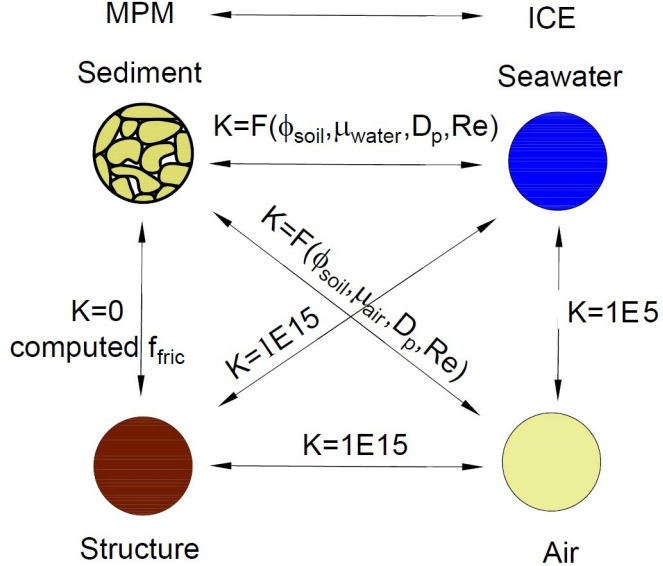


Figure 3: Momentum exchange coefficient between materials

291 Solving momentum and energy exchange with an implicit solver

292 The derivation of the implicit integration for the momentum exchange is  
 293 presented in the Appendix's section 'Momentum and energy exchange with  
 294 an implicit solver'. The linear equations for multi phases  $i,j=1:N$  has the  
 295 form as:

$$\begin{vmatrix} (1 + \beta_{ij}) & -\beta_{ij} \\ -\beta_{ji} & (1 + \beta_{ji}) \end{vmatrix} \begin{vmatrix} \Delta \mathbf{U}_i \\ \Delta \mathbf{U}_j \end{vmatrix} = \begin{vmatrix} \beta_{ij} (\mathbf{U}_i^* - \mathbf{U}_j^*) \\ \beta_{ji} (\mathbf{U}_i^* - \mathbf{U}_j^*) \end{vmatrix}$$

296 where the intermediate velocity for fluid phases  $f=1:N_f$  and for solid/porous  
 297 phases  $s=1:N_s$  can be calculated by:

$$\begin{aligned} \mathbf{U}_f^* &= \mathbf{U}_f^n + \Delta t \left( -\frac{\nabla P_f^{n+1}}{\rho_f^n} + \frac{\nabla \cdot \boldsymbol{\tau}_f^n}{\bar{\rho}_f^n} + \mathbf{b} \right) \\ \mathbf{U}_s^* &= \mathbf{U}_s^n + \Delta t \left( \frac{\nabla \cdot \boldsymbol{\sigma}'^n}{\bar{\rho}_s^n} - \frac{\nabla P_f^{n+1}}{\rho_s} + \mathbf{b} \right) \end{aligned} \quad (33)$$

298 Also, the momentum exchange coefficient can be computed at every time  
 299 step as  $\beta_{12} = K/\bar{\rho}_f^n$  and  $\beta_{21} = K/\bar{\rho}_s^n$  with the coefficient depending on the  
 300 different type of interactions (see Figure 3) as for example:

301

- 302 1. The drag force is set to zero in soil-structure interactions, and instead  
 303 the frictional force is computed.  
 304 2. As a result of fluid-structure interaction, the momentum exchange coef-  
 305 ficient should be extremely high (1E15) when the solid material points  
 306 are considered to be zero-porosity/zero-permeability.  
 307 3. In the case of soil-fluid interaction, the drag force is calculated using  
 308 the equation (25). Considering that air has a much lower viscosity than  
 309 water, its drag force is much lower than the drag force of water in a  
 310 pore.  
 311 4. A momentum exchange coefficient of 1E5 is applied between multiphase  
 312 flows. This value is far higher than reality [24], but it is necessary to  
 313 have enough numerical stability to conduct simulations in the numerical  
 314 example.

315 Similar approach applied for the energy exchange term leading to:

$$\begin{vmatrix} (1 + \eta_{ij}) & -\eta_{ij} \\ -\eta_{ji} & (1 + \eta_{ji}) \end{vmatrix} \begin{vmatrix} \Delta T_i \\ \Delta T_j \end{vmatrix} = \begin{vmatrix} \eta_{ij}(T_i^n - T_j^n) \\ \eta_{ji}(T_j^n - T_i^n) \end{vmatrix}$$

316 with  $\eta$  being the energy exchange coefficient.

317 *Equation of state for fluid phases*

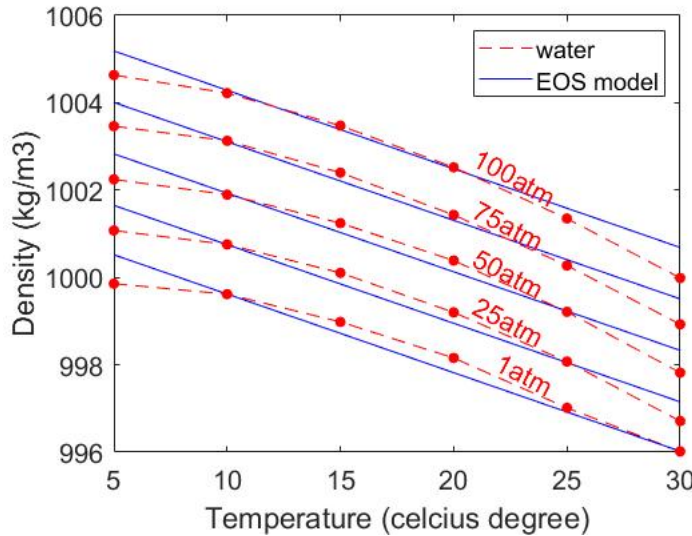


Figure 4: Equation of state of water

318     The equation of state establishes relations between thermodynamics vari-  
 319     ables  $[P_f, \rho_f, T_f]$ . The choice of the equation of state depends on the types  
 320     of the fluid materials. For example, for the air, it is possible to assume the  
 321     equation of state for the perfect gas which obeys:

$$P_f = \rho_f R T_f \quad (34)$$

322     where  $R$  is the gas constant. For the water, a simple linear equation of state  
 323     is in the following form:

$$P_f = P_{ref} + K_f(\rho_f - \rho_{ref} + \alpha_f(T_f - T_{ref})) \quad (35)$$

324     where reference pressure  $P_{ref} = 1 \text{ atm} = 101325 \text{ Pa}$ , reference temperature  
 325      $T_{ref} = 10^\circ\text{C}$ , reference density  $\rho_{ref} = 999.8 \text{ kg/m}^3$ , the bulk modulus of water  
 326      $K_f = 2 \text{ GPa}$ , and the water thermal expansion  $\alpha_f = 0.18 \text{ }^\circ\text{C}^{-1}$ . Equation  
 327     (35) matches well with the state of the water (see Figure 4).

### 328     Numerical implementation

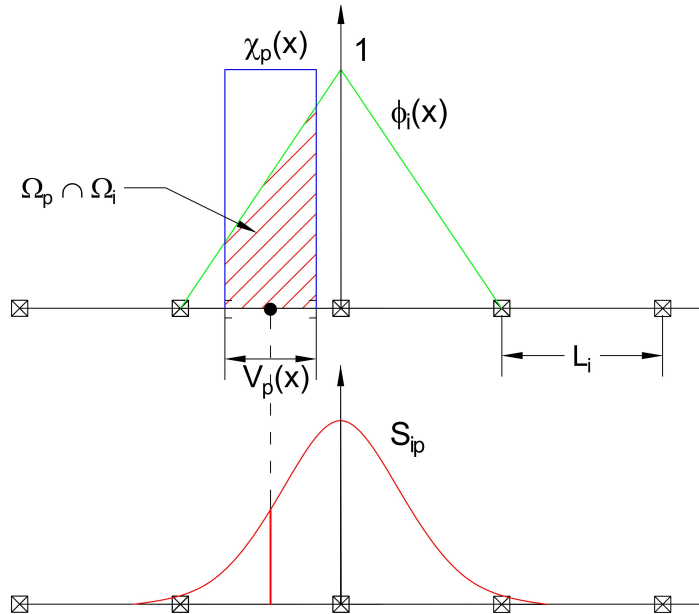


Figure 5: GIMP weighting function (red as a convolution of the linear basis shape function (green) and the characteristic function (blue))

329     The fluid phases are discretized in the grid with the state variables stored  
 330    at the centroid of the cells  $[\rho_{f,c}, \mathbf{U}_{f,c}, T_{f,c}, v_{f,c}]$  while the solid phase is dis-  
 331    cretized in the particles with the state variables  $[m_{sp}, \mathbf{U}_{sp}, T_{sp}, \boldsymbol{\sigma}'_{sp}]$ . In the  
 332    Material Point Method, we use the generalized interpolation technique [25]  
 333    using the weight function as a convolution of a grid shape function  $N_i(\mathbf{x})$  in  
 334    a nodal domain  $\Omega_i$  and a characteristic function  $\chi_p(\mathbf{x})$  in a particle domain  
 335     $\Omega_p$  with the volume  $V_p(\mathbf{x})$  as follows:

$$S_{ip} = \frac{1}{V_p} \int_{\Omega_i \cap \Omega_p} N_i(\mathbf{x}) \chi_p(\mathbf{x}) d\mathbf{x} \quad (36)$$

336    where the volume  $V_p(\mathbf{x})$  of the material point p can be calculated as:

$$V_p = \int_{\Omega_p} \chi_p(\mathbf{x}) d\mathbf{x} \quad (37)$$

337    The characteristic function is the Heaviside function as  $\chi_p = 1$  if  $\mathbf{x} \in \Omega_p$ ,  
 338    otherwise 0 (see Figure 5). For the interpolation of the centroid of the cell,  
 339    the linear basis function is used as:

$$S_{ci} = N_i(\mathbf{x}_c) \quad (38)$$

340    The time discretization are solved using the following steps.

341    *Interpolation from Solid Particle to Grid*

342    The nodal values of the solid state (mass, velocity, temperature, volume)  
 343    are:

$$\begin{aligned} m_{si}^n &= \sum S_{ip} m_{sp} \\ \mathbf{U}_{si}^n &= \frac{\sum S_{ip} (m\mathbf{U})_{sp}^n}{m_{si}^n} \\ T_{si}^n &= \frac{\sum S_{ip} (mT)_{sp}^n}{m_{si}^n} \\ V_{si}^n &= \frac{\sum S_{ip} (mV)_{sp}^n}{m_{si}^n} \\ \boldsymbol{\sigma}_{si}^n &= \frac{\sum S_{ip} (\boldsymbol{\sigma}V)_{sp}^n}{V_{si}^n} \end{aligned} \quad (39)$$

344    The nodal internal forces is calculated by:

$$\mathbf{f}_{si}^{int,n} = - \sum \nabla S_{ip} (\boldsymbol{\sigma}'_{sp})^n V_{sp}^n \quad (40)$$

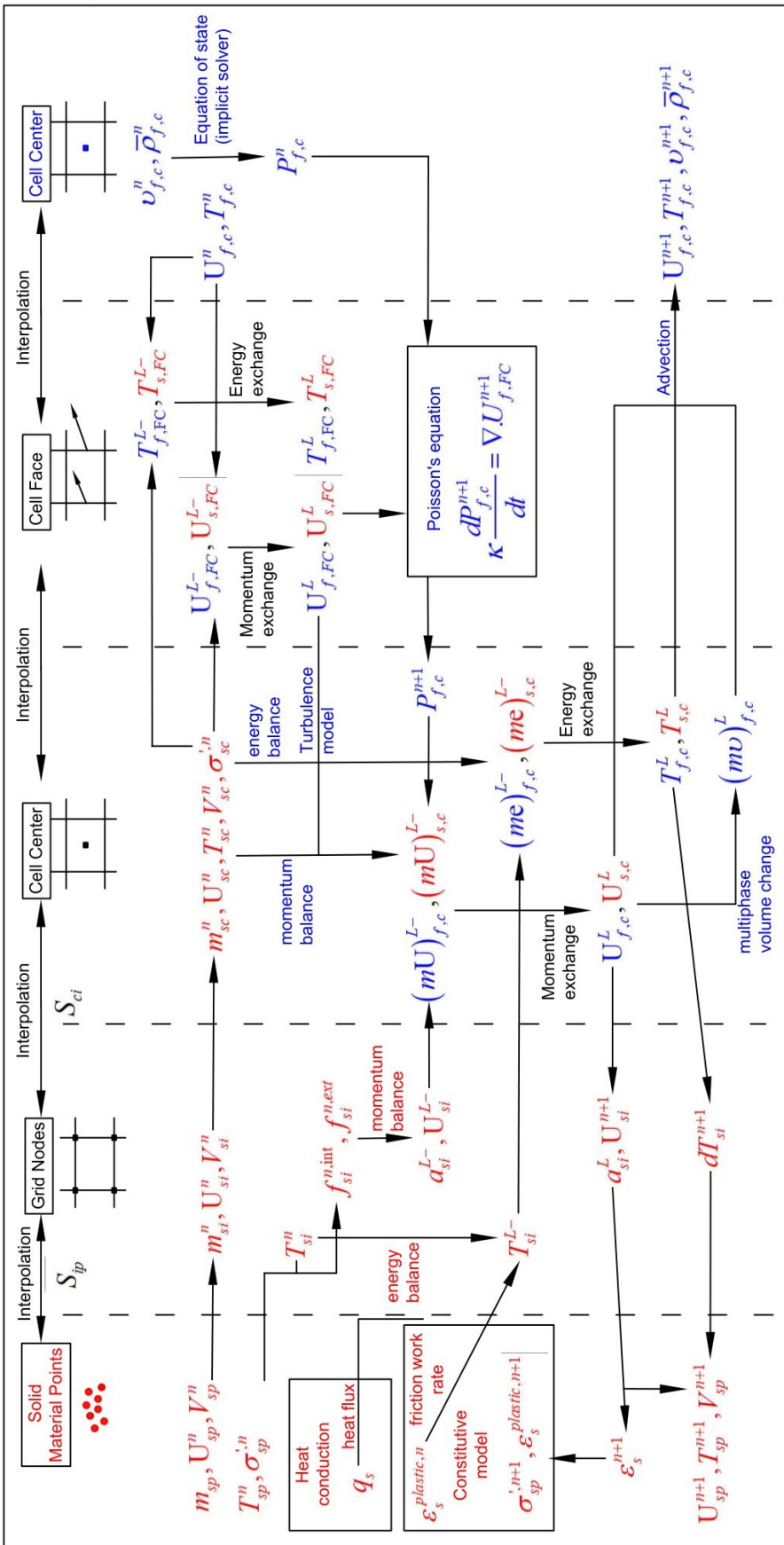


*Figure 6: Numerical implementation of MPMICE*

345 The nodal external forces  $f_{si}^{ext,n}$  and the frictional forces from soil-structure  
 346 interaction  $f_{fric,si}^n$  from contact between materials are computed here.  
 347 Then we compute the solid cell variables as:

$$\begin{aligned} m_{sc}^n &= \sum S_{ci} m_{si} \\ \rho_{sc}^n &= \frac{m_{sc}^n}{V} \\ \mathbf{U}_{sc}^n &= \sum S_{ci} \mathbf{U}_{si}^n \\ T_{sc}^n &= \sum S_{ci} T_{si}^n \\ V_{sc}^n &= \sum S_{ci} V_{si}^n \\ \boldsymbol{\sigma}_{sc}^n &= \sum S_{ci} \boldsymbol{\sigma}_{si}^n \end{aligned} \tag{41}$$

348 *Compute equation of state for fluid phase*

349 The total fluid material volume of a cell is:

$$V_{total} = \sum_{f=1}^{N_f} M_f v_f \tag{42}$$

350 We need to find  $P_{f,c}^n$  which allows each fluid materials obey their equation of  
 351 states  $[P_f, \rho_f, v_f, T_f, e_f]$  but also allow mass of all fluid materials to fill the  
 352 entire the pore volume without ongoing compression or expansion following  
 353 the condition as follows:

$$0 = n - \sum_{f=1}^{N_f} v_f \bar{\rho}_f \tag{43}$$

354 Then, we can use the Newton-Raphson interation to find the value of  $P_{f,c}^n$   
 355 which satisfies the equation (42, 43) and each equation of states of each fluid  
 356 materials.

357 *Compute cell face velocity*

358 Following the derivation in the Appendix: Advanced Fluid Pressure, we  
 359 first compute the fluid cell face velocity as:

$$\mathbf{U}_{f,FC}^{L-} = \frac{(\bar{\rho} \mathbf{U})_{f,FC}^n}{\bar{\rho}_{f,FC}^n} + \Delta t \left( -\frac{\nabla^{FC} P_{f,c}^n}{\rho_{f,FC}^n} + \frac{\nabla^{FC} \cdot \boldsymbol{\tau}^n}{\bar{\rho}_{s,FC}} + \mathbf{b} \right) \tag{44}$$

<sup>360</sup> The equation (44) is discretized in three dimension (noted that  $\nabla^{FC} \cdot \boldsymbol{\tau} = 0$ ),  
<sup>361</sup> for example the discretized equation in the x direction is:

$$U_{fx}^{L-} = \frac{(\bar{\rho}U)_{fx,R}^n + (\bar{\rho}U)_{fx,L}^n}{\bar{\rho}_{fx,L}^n + \bar{\rho}_{fx,R}^n} + \Delta t \left( -\frac{2(v_{fx,L}^n v_{fx,R}^n)}{v_{fx,L}^n + v_{fx,R}^n} \frac{P_{f,cx,R}^n - P_{f,cx,L}^n}{\Delta x} + b_x \right) \quad (45)$$

<sup>362</sup> The cell face solid velocity can be calculated as:

$$\mathbf{U}_{s,FC}^{L-} = \frac{(\bar{\rho}\mathbf{U})_{s,FC}^n}{\bar{\rho}_{s,FC}^n} + \Delta t \left( \frac{\nabla^{FC} \cdot \boldsymbol{\sigma}_c'^n}{\bar{\rho}_{s,FC}} - \frac{\nabla^{FC} P_{f,c}^n}{\rho_s} + \mathbf{b} \right) \quad (46)$$

<sup>363</sup> The equation (46) is discretized in three dimension (noted that  $\nabla^{FC} \cdot \boldsymbol{\sigma}_{ij} = 0$   
<sup>364</sup> with  $i \neq j$ ), for example the discretized equation in the x direction is:

$$U_{sx}^{L-} = \frac{(\bar{\rho}U)_{sx,R}^n + (\bar{\rho}U)_{sx,L}^n}{\bar{\rho}_{sx,L}^n + \bar{\rho}_{sx,R}^n} + \Delta t \left( \frac{2(\sigma_{xx,R} - \sigma_{xx,L})}{(\bar{\rho}_{sx,L}^n + \bar{\rho}_{sx,R}^n) \Delta x} - \frac{P_{f,cx,R}^n - P_{f,cx,L}^n}{\rho_s \Delta x} + b_x \right) \quad (47)$$

<sup>365</sup> Then, we compute the modified cell face velocity  $\mathbf{U}_{FC}^L$  considering the mo-  
<sup>366</sup> mentum exchange (see the Appendix: Momentum exchange with an implicit  
<sup>367</sup> solve) as follows:

$$\begin{aligned} \mathbf{U}_{f,FC}^L &= \mathbf{U}_{f,FC}^{L-} + \Delta \mathbf{U}_{f,FC} \\ \mathbf{U}_{s,FC}^L &= \mathbf{U}_{s,FC}^{L-} + \Delta \mathbf{U}_{s,FC} \end{aligned} \quad (48)$$

<sup>368</sup> The linear equation below is solved to obtain the increment of velocity with  
<sup>369</sup> i,j = 1 : N as:

$$\begin{vmatrix} (1 + \beta_{ij}) & -\beta_{ij} \\ -\beta_{ji} & (1 + \beta_{ji}) \end{vmatrix} \begin{vmatrix} \Delta \mathbf{U}_{i,FC} \\ \Delta \mathbf{U}_{j,FC} \end{vmatrix} = \begin{vmatrix} \beta_{ij} (\mathbf{U}_{i,FC}^{L-} - \mathbf{U}_{j,FC}^{L-}) \\ \beta_{ji} (\mathbf{U}_{j,FC}^{L-} - \mathbf{U}_{i,FC}^{L-}) \end{vmatrix}$$

### <sup>370</sup> Compute cell face temperature

<sup>371</sup> Similar to the velocity, the faced temperature is computed, for example  
<sup>372</sup> in x direction, as:

$$\begin{aligned} T_{fx}^{L-} &= \frac{(\bar{\rho}T)_{fx,R}^n + (\bar{\rho}T)_{fx,L}^n}{\bar{\rho}_{fx,L}^n + \bar{\rho}_{fx,R}^n} \\ T_{sx}^{L-} &= \frac{(\bar{\rho}T)_{sx,R}^n + (\bar{\rho}T)_{sx,L}^n}{\bar{\rho}_{sx,L}^n + \bar{\rho}_{sx,R}^n} \end{aligned} \quad (49)$$

<sup>373</sup> Then, we compute the modified cell face temperature  $T_{FC}^L$  considering the  
<sup>374</sup> energy exchange (see the Appendix: Momentum and energy exchange with

<sup>375</sup> an implicit solver) as follows:

$$\begin{aligned} T_{f,FC}^L &= T_{f,FC}^{L-} + \Delta T_{f,FC} \\ T_{s,FC}^L &= T_{s,FC}^{L-} + \Delta T_{s,FC} \end{aligned} \quad (50)$$

<sup>376</sup> The linear equation below is solved to determine the increment of tempera-  
<sup>377</sup> ture due to energy exchange with  $i,j = 1 : N$  as:

$$\begin{vmatrix} (1 + \eta_{ij}) & -\eta_{ij} \\ -\eta_{ji} & (1 + \eta_{ji}) \end{vmatrix} \begin{vmatrix} \Delta T_{i,FC} \\ \Delta T_{j,FC} \end{vmatrix} = \begin{vmatrix} \eta_{ij}(T_{i,FC}^{L-} - T_{j,FC}^{L-}) \\ \eta_{ji}(T_{j,FC}^{L-} - T_{i,FC}^{L-}) \end{vmatrix}$$

<sup>378</sup> *Compute fluid pressure (implicit scheme)*

<sup>379</sup> For single phase flow, the increment of the fluid pressure can be computed  
<sup>380</sup> as:

$$\kappa_f \frac{\Delta P}{dt} = \nabla^c \cdot \mathbf{U}_{f,FC}^{n+1} \quad (51)$$

<sup>381</sup> For multi-phase flows, the increment of the fluid pressure of the mixture can  
<sup>382</sup> be computed as:

$$\kappa \frac{\Delta P}{dt} = \sum_{f=1}^{N_f} \nabla^c \cdot (\phi_{f,FC} \mathbf{U}_{f,FC})^{n+1} \quad (52)$$

<sup>383</sup> where  $\kappa = \sum_{f=1}^{N_f} (\phi_{f,FC} \kappa_f) / \sum_{f=1}^{N_f} (\phi_{f,FC})$ . Then, the fluid pressure at cell  
<sup>384</sup> center is:

$$P_c^{n+1} = P_c^n + \Delta P_c^n \quad (53)$$

<sup>385</sup> Finally, the cell face advanced fluid pressure is:

$$P_{FC}^{n+1} = \left( \frac{P_{c,L}^{n+1}}{\bar{\rho}_{f,L}^n} + \frac{P_{c,R}^{n+1}}{\bar{\rho}_{f,R}^n} \right) / \left( \frac{1}{\bar{\rho}_{f,L}^n} + \frac{1}{\bar{\rho}_{f,R}^n} \right) = \left( \frac{P_{c,L}^{n+1} \bar{\rho}_{f,R}^n + P_{c,R}^{n+1} \bar{\rho}_{f,L}^n}{\bar{\rho}_{f,L}^n \bar{\rho}_{f,R}^n} \right) \quad (54)$$

<sup>386</sup> *Compute viscous shear stress term of the fluid phase*

<sup>387</sup> This part compute the viscous shear stress  $\Delta(m\mathbf{U})_{f,c,\tau}$  for a single vis-  
<sup>388</sup> cous compressible Newtonian fluid and optionally shear stress induced by the  
<sup>389</sup> turbulent model.

390    *Compute nodal internal temperature of the solid phase*

391    The nodal internal temperature rate is computed based on the heat con-  
 392    duction model as below:

$$dT_{si}^{L-} = \frac{(\Delta W_{si}^n + \Delta W_{fric,i}^n + \nabla^i \cdot \mathbf{q}_{si}^n)}{m_{si}^n c_v} \quad (55)$$

393    where  $\Delta W_{si}^n = \boldsymbol{\sigma}' : \frac{D_s(\boldsymbol{\epsilon}_s^p)}{Dt}$  is the mechanical work rate computed from the  
 394    constitutive model with  $\boldsymbol{\epsilon}_s^p$  is the plastic strain,  $\Delta W_{fric,i}^n$  is the work rate  
 395    computed from the contact law due to the frictional sliding between solid  
 396    materials. The heat flux is  $\mathbf{q}_s = \bar{\rho}_s \beta_s \nabla T_s$  with  $\beta_s$  being the thermal conduc-  
 397    tivity of the solid materials.

$$T_{si}^{L-} = T_{si}^n + dT_{si}^{L-} \quad (56)$$

398    *Compute and integrate acceleration of the solid phase*

399    After interpolating from material points to the nodes, the nodal acceler-  
 400    ation and velocity are calculated by:

$$\mathbf{a}_{si}^{L-} = \frac{\mathbf{f}_{si}^{int,n} + \mathbf{f}_{si}^{ext,n}}{m_{si}^n} + \mathbf{g} \quad (57)$$

$$\mathbf{U}_{si}^{L-} = \mathbf{U}_{si}^n + \mathbf{a}_{si}^{L-} \Delta t \quad (58)$$

402    *Compute Lagrangian value (mass, momentum and energy)*

403    For the fluid phase, the linear momentum rate, the energy rate are:

$$\Delta(m\mathbf{U})_{f,c} = V n_c^n \nabla^c P_c^{n+1} + \Delta(m\mathbf{U})_{f,c,\tau} + V \bar{\rho}_{f,c}^n g \quad (59)$$

$$\Delta(me)_{f,c} = V n_c^n P_c^{n+1} \nabla^c \cdot \mathbf{U}_{f,FC}^* + \nabla^c \cdot \mathbf{q}_{f,c}^n \quad (60)$$

405    The heat flux is  $\mathbf{q}_f = \bar{\rho}_f \beta_f \nabla T_f$  with  $\beta_f$  being the thermal conductivity of the  
 406    fluid materials. The Lagrangian value of the mass, linear momentum and  
 407    energy of fluid phases without momentum exchange are:

$$m_{f,c}^L = V \bar{\rho}_{f,c}^n \quad (61)$$

$$(m\mathbf{U})_{f,c}^{L-} = V \bar{\rho}_{f,c}^n \mathbf{U}_{f,c}^n + \Delta(m\mathbf{U})_{f,c} \quad (62)$$

$$(me)_{f,c}^{L-} = V \bar{\rho}_{f,c}^n T_{f,c}^n c_v + \Delta(me)_{f,c} \quad (63)$$

<sup>410</sup> For the solid phase, the Lagrangian value of the linear momentum and energy  
<sup>411</sup> of solid phase are:

$$m_{sc}^L = m_{sc}^n \quad (64)$$

$$(m\mathbf{U})_{sc}^{L-} = \sum S_{ci} m_{si}^n \mathbf{U}_{si}^{L-} + V(1 - n_c^n) \nabla^c P_{f,c}^{n+1} \quad (65)$$

$$(me)_{sc}^{L-} = \sum S_{ci} m_{si}^n T_{si}^L c_v \quad (66)$$

<sup>414</sup> To consider the momentum exchange, the Lagrangian velocity is modified as:

$$\begin{aligned} \mathbf{U}_{f,c}^L &= \mathbf{U}_{f,c}^{L-} + \Delta \mathbf{U}_{f,c} \\ \mathbf{U}_{sc}^L &= \mathbf{U}_{sc}^{L-} + \Delta \mathbf{U}_{sc} \end{aligned} \quad (67)$$

<sup>415</sup> where the cell-centered intermediate velocity can be calculated by:

$$\begin{aligned} \mathbf{U}_{f,c}^{L-} &= \frac{(m\mathbf{U})_{f,c}^{L-}}{m_{f,c}^L} \\ \mathbf{U}_{sc}^{L-} &= \frac{(m\mathbf{U})_{sc}^{L-}}{m_{sc}^L} \end{aligned} \quad (68)$$

<sup>416</sup> And the increment of the velocity  $\mathbf{U}_{f,c}$ ,  $\Delta \mathbf{U}_{sc}$  can be computed by solving  
<sup>417</sup> the linear equation with  $i,j = 1:N$  as:

$$\begin{vmatrix} (1 + \beta_{ij}) & -\beta_{ij} \\ -\beta_{ji} & (1 + \beta_{ji}) \end{vmatrix} \begin{vmatrix} \Delta \mathbf{U}_{i,c} \\ \Delta \mathbf{U}_{j,c} \end{vmatrix} = \begin{vmatrix} \beta_{ij} (\mathbf{U}_{i,c}^{L-} - \mathbf{U}_{j,c}^{L-}) \\ \beta_{ji} (\mathbf{U}_{j,c}^{L-} - \mathbf{U}_{i,c}^{L-}) \end{vmatrix}$$

<sup>418</sup> To consider the energy exchange, the Lagrangian temperature is modified as:

$$\begin{aligned} T_{f,c}^L &= T_{f,c}^{L-} + \Delta T_{f,c} \\ T_{sc}^L &= T_{sc}^{L-} + \Delta T_{sc} \end{aligned} \quad (69)$$

<sup>419</sup> where the cell-centered intermediate temperature can be calculated by:

$$\begin{aligned} T_{f,c}^{L-} &= \frac{(mT)_{f,c}^{L-}}{m_{f,c}^L c_v} \\ T_{sc}^{L-} &= \frac{(mT)_{sc}^{L-}}{m_{sc}^L c_v} \end{aligned} \quad (70)$$

<sup>420</sup> And the increment of the temperature due to energy exchange can be com-  
<sup>421</sup> puted by solving the linear equation with  $i,j = 1:N$  as:

$$\begin{vmatrix} (1 + \eta_{ij}) & -\eta_{ij} \\ -\eta_{ji} & (1 + \eta_{ji}) \end{vmatrix} \begin{vmatrix} \Delta T_{i,c} \\ \Delta T_{j,c} \end{vmatrix} = \begin{vmatrix} \eta_{ij} (T_{i,c}^{L-} - T_{j,c}^{L-}) \\ \eta_{ji} (T_{j,c}^{L-} - T_{i,c}^{L-}) \end{vmatrix}$$

422 Finally, we obtain the cell-centered solid acceleration and temperature rate  
 423 as:

$$d\mathbf{U}_{sc}^L = \frac{(m\mathbf{U})_{sc}^L - (m\mathbf{U})_{sc}^n}{m_{sc}^L \Delta t} \quad (71)$$

$$dT_{sc}^L = \frac{(me)_{sc}^L - (me)_{sc}^n}{m_{sc}^L c_v \Delta t} \quad (72)$$

425 *Compute Lagrangian specific volume of the fluid phase*

426 To compute the Lagrangian value of the specific volume of the fluid phase,  
 427 we need to compute the Lagrangian temperature rate as below:

$$T_{f,c}^{n+1} = \frac{(me)_{f,c}^L}{m_{f,c}^L c_v} \quad (73)$$

$$\frac{D_f T_{f,c}}{Dt} = \frac{T_{f,c}^{n+1} - T_{f,c}^n}{\Delta t} \quad (74)$$

429 As such, the Lagrangian specific volume rate is:

$$\Delta(mv)_{f,c} = V f_{f,c}^\phi \nabla \cdot \mathbf{U} + (\phi_{f,c} \alpha_{f,c} \frac{D_f T_{f,c}}{Dt} - f_{f,c}^\phi \sum_{n=1}^N \phi_{nc} \alpha_{nc} \frac{D_n T_{n,c}}{Dt}) \quad (75)$$

430 where  $f_f^\phi = (\phi_f \kappa_f) / (\sum_{n=1}^N \phi_n \kappa_n)$  and  $\mathbf{U} = \nabla \cdot (\sum_{s=1}^{N_s} \phi_{sc} \mathbf{U}_{sc} + \sum_{f=1}^{N_f} \phi_{fc} \mathbf{U}_{f,c})$ .  
 431 Finally, the Lagrangian specific volume is:

$$(mv)_{f,c}^L = V \bar{\rho}_{f,c}^n v_{f,c}^n + \Delta(mv)_{f,c} \quad (76)$$

432 *Compute advection term and advance in time*

433 The mass, linear momentum, energy and specific volume with advection  
 434 are:

$$m_{f,c}^{n+1} = m_{f,c}^L - \Delta t \nabla \cdot (\bar{\rho}_{f,c}^L, \mathbf{U}_{f,FC}^L) \quad (77)$$

$$(m\mathbf{U})_{f,c}^{n+1} = (m\mathbf{U})_{f,c}^L - \Delta t \nabla \cdot ((\bar{\rho}\mathbf{U})_{f,c}^L, \mathbf{U}_{f,FC}^L) \quad (78)$$

$$(me)_{f,c}^{n+1} = (me)_{f,c}^L - \Delta t \nabla \cdot ((\bar{\rho}c_v T)_{f,c}^L, \mathbf{U}_{f,FC}^L) \quad (79)$$

$$(mv)_{f,c}^{n+1} = (mv)_{f,c}^L - \Delta t \nabla \cdot ((\bar{\rho}v)_{f,c}^L, \mathbf{U}_{f,FC}^L) \quad (80)$$

437 Finally, the state variables of the fluid phases of the next time step are:

$$\bar{\rho}_{f,c}^{n+1} = \frac{m_{f,c}^{n+1}}{V} \quad (81)$$

439

$$\mathbf{U}_{f,c}^{n+1} = \frac{(m\mathbf{U})_{f,c}^{n+1}}{m_{f,c}^{n+1}} \quad (82)$$

440

$$T_{f,c}^{n+1} = \frac{(me)_{f,c}^{n+1}}{m_{f,c}^{n+1}} \quad (83)$$

441

$$v_{f,c}^{n+1} = \frac{(mv)_{f,c}^{n+1}}{m_{f,c}^{n+1}} \quad (84)$$

442 *Interpolate from cell to node of the solid phase*443 First we interpolate the acceleration, velocity and temperature rate to  
444 the node as below:

445 
$$\mathbf{a}_{si}^n = \sum S_{ci} d\mathbf{U}_{sc}^L \quad (85)$$

446 
$$\mathbf{U}_{si}^{n+1} = \sum S_{ci} d\mathbf{U}_{sc}^L \Delta t \quad (86)$$

447 
$$dT_{si}^n = \sum S_{ci} dT_{sc}^L \quad (87)$$

448 Then the boundary condition and contact forces  $f_{si}^{fric}$  are applied to the nodal  
velocity, and then accelerations are modified by:

449 
$$\mathbf{a}_{si}^n = \frac{\mathbf{v}_{si}^{n+1} - \mathbf{v}_{si}^n}{\Delta t} \quad (88)$$

450 *Update the particle variables*451 The state variables of the solid phase  $[\mathbf{U}_{sp}^{n+1}, \mathbf{x}_{sp}^{n+1}, \nabla \mathbf{U}_{sp}^{n+1}, T_{sp}^{n+1}, \nabla T_{sp}^{n+1}, \mathbf{F}_{sp}^{n+1}, V_{sp}^{n+1}]$   
452 (velocity, position, velocity gradient, temperature, temperature gradient, de-  
formation gradient, volume) are updated as:

453 
$$\mathbf{U}_{sp}^{n+1} = \mathbf{U}_{sp}^n + \sum S_{sp} \mathbf{a}_{si}^n \Delta t \quad (89)$$

454 
$$\mathbf{x}_{sp}^{n+1} = \mathbf{x}_{sp}^n + \sum S_{sp} \mathbf{U}_{si}^{n+1} \Delta t \quad (90)$$

455 
$$\nabla \mathbf{U}_{sp}^{n+1} = \sum \nabla S_{sp} \mathbf{U}_{si}^{n+1} \quad (91)$$

456 
$$T_{sp}^{n+1} = T_{sp}^n + \sum S_{sp} dT_{si}^n \Delta t \quad (92)$$

$$\nabla T_{sp}^{n+1} = \sum \nabla S_{sp} T_{sp}^n \Delta t \quad (93)$$

457                    $\mathbf{F}_{sp}^{n+1} = (\mathbf{I} + \nabla \mathbf{U}_{sp}^{n+1} \Delta t) \mathbf{F}_{sp}^n$                    (94)

458                    $V_{sp}^{n+1} = \det(\mathbf{F}_{sp}^{n+1}) V_{sp}^o$                    (95)

459       Finally, the effective stress  $(\sigma')^{n+1}$  is updated from the constitutive model  
460       and the pore water pressure is interpolated from the cell as:

461                    $p_f^{n+1} = \sum S_{si} P_c^{n+1}$                    (96)

## 461       Numerical examples

462       All input files and the analytical calculations in this section are provided  
463       in the Github repository ([https://github.com/QuocAnh90/Uintah\\_NTNU](https://github.com/QuocAnh90/Uintah_NTNU))  
464       for the reproduction of the numerical results.

465       To prevent repetition, we present the parameters of water and air, which  
466       remain consistent across all simulations. The water has a bulk modulus of 2  
467       GPa, a density of 998 kg/m<sup>3</sup> at a reference temperature of 5 degrees Celsius  
468       and a reference pressure of 10325 Pa (1atm), a dynamic viscosity  $\mu_f$  of 1  
469       mPa s). The air has a ideal gas with a density of 1.17 kg/m<sup>3</sup> at a reference  
470       temperature of 5 degrees Celsius and a reference pressure of 10325 Pa (1atm),  
471       a dynamic viscosity  $\mu_f$  of  $18.45E^{-3}$  mPa s).

### 472       Fluid Flow through isothermal porous media

473       Fluid flow through porous media is important in many engineering disci-  
474       plines, like predicting water flow in soil. Fluid flow velocity in one dimension  
475       can be calculated from the porous media's hydraulic conductivity  $K$  as:

476                    $U_f = K \frac{\Delta p_f}{L}$                    (97)

477       If the Carman-Kozeny formula is adopted  $F = 10\phi_s/(1 - \phi_s)^2$ , the hydraulic  
478       conductivity will be expressed as  $K = D_p^2(1 - \phi_s)^3 \rho_f g / 180\phi_s^2 \mu_f$ . Then, the  
479       analytical formula of average velocity in one dimension through the porous  
480       media is:

481                    $U_f = \frac{1}{n} \frac{D_p^2(1 - \phi_s)^3}{180\phi_s^2 \mu_f} \frac{\Delta p_f}{L}$                    (98)

482       Our numerical model is validated by modeling fluid flow through a 1m  
483       long porous media. The porous media is modeled by elastic material with

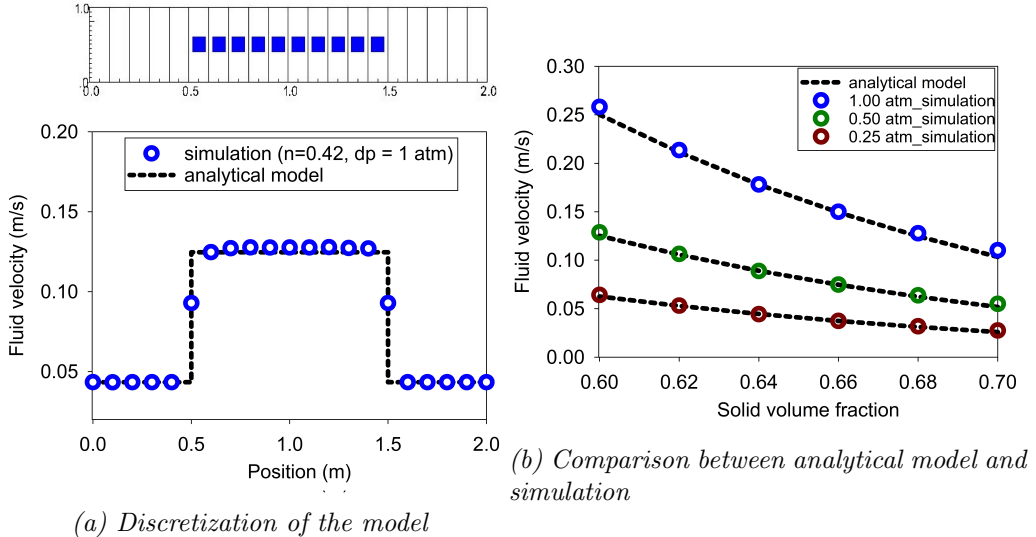


Figure 7: Numerical results of the fluid flow through isothermal porous media

484 Young's modulus is 10 MPa, Poisson's ratio is 0.3, and density is 2650 kg/m<sup>3</sup>.  
 485 The volume fraction of porous media  $\phi_s$  is [0.6, 0.62, 0.66, 0.68, 0.7] and the  
 486 average grain diameter  $d$  is 1mm. The model is discretized in 20 finite element  
 487 and the porous media in 10 finite element with 1 material point per element.  
 488 The pressure gradient is applied with three different value [0.25, 0.5, 1] atm.  
 489 Figure 7 shows a good agreement of fluid flow prediction between the theory  
 490 and the model.

#### 491 Isothermal consolidation

492 A common benchmark for a fully saturated porous media is the simulation  
 493 of one-dimensional consolidation. Using the Carman-Kozeny formula, the  
 494 time-dependent pressure can be calculated as:

$$495 \quad p_f = \sum_{m=1}^{\infty} \frac{2F_{ext}}{M} \sin\left(\frac{Mz}{H}\right) e^{-M^2 T_V} \text{ with } M = \frac{\pi}{2}(2m+1) \quad (99)$$

496 where the consolidation rate  $T_v = C_v t / H^2$ , the consolidation coefficient  $C_v =$   
 497  $E_v n^3 d^2 / (180(1-n)^2 \mu)$  and the Oedometer modulus  $E_v = E(1-v)/(1+v)/(1-2v)$ . Our numerical model is validated by modeling the consolidation  
 498 of a 1m column. The porous media is modeled by elastic material with  
 499 Young's modulus is 10 MPa, Poisson's ratio is 0.3, and density is 2650 kg/m<sup>3</sup>.

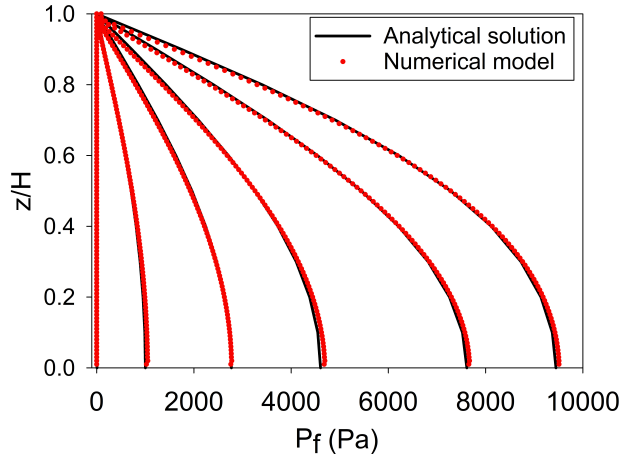


*Figure 8: Comparison between analytical solution and numerical solution*

500 The volume fraction of porous media  $\phi_s$  is 0.7 which is equivalent to the  
 501 porosity of 0.3 and the average grain diameter  $d$  is 1mm. The model is  
 502 discretized in 100 finite element with 1 material point per element. The  
 503 external pressure applies to the top of the column is 10 kPa. Figure 8 shows  
 504 a good agreement of fluid flow prediction between the theory and the model.

505 *Thermal induced cavity flow*

506 Another benchmark is the thermal induced cavity flow in porous me-  
 507 dia. Temperature and velocity distributions are calculated for a square non-  
 508 deformable saturated porous media. The top and bottom walls are insulated,  
 509 and the left and right walls are at fixed temperature gradient of 1 degree. The  
 510 fluid motion at steady state are cavity flow due to the temperature induced  
 511 density variation. The numerical is validated by comparing with the numer-  
 512 ical solution of the finite element method. The porous media is modeled  
 513 by non deformable material, and density is 2500 kg/m<sup>3</sup>. The specific heat  
 514 capacity of the water and porous skeleton are 4181 J/kg.K and 835 J/kg.K  
 515 respectively. The thermal conductivity of the water and porous skeleton are  
 516 0.598 W/m.K and 0.4 W/m.K. The volume fraction of porous media  $\phi_s$  is 0.6  
 517 which is equivalent to the porosity of 0.4 and the average grain diameter  $d$  is  
 518 1mm. The model is discretized in 20 x 20 finite element with 4 material point  
 519 per element. Figure 10 shows a good agreement of numerical results of the  
 520 model compared with the numerical solution of the finite element method.

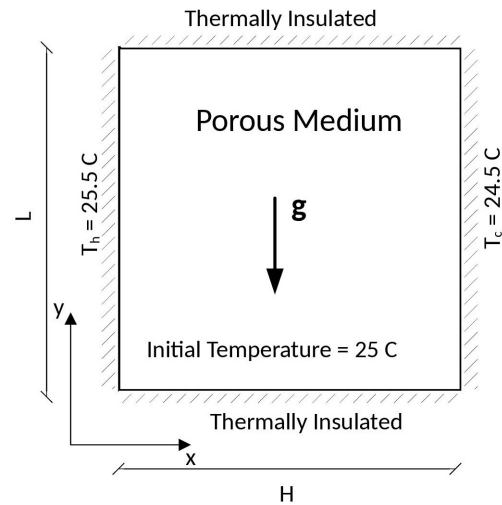


Figure 9: Model schematic [26]

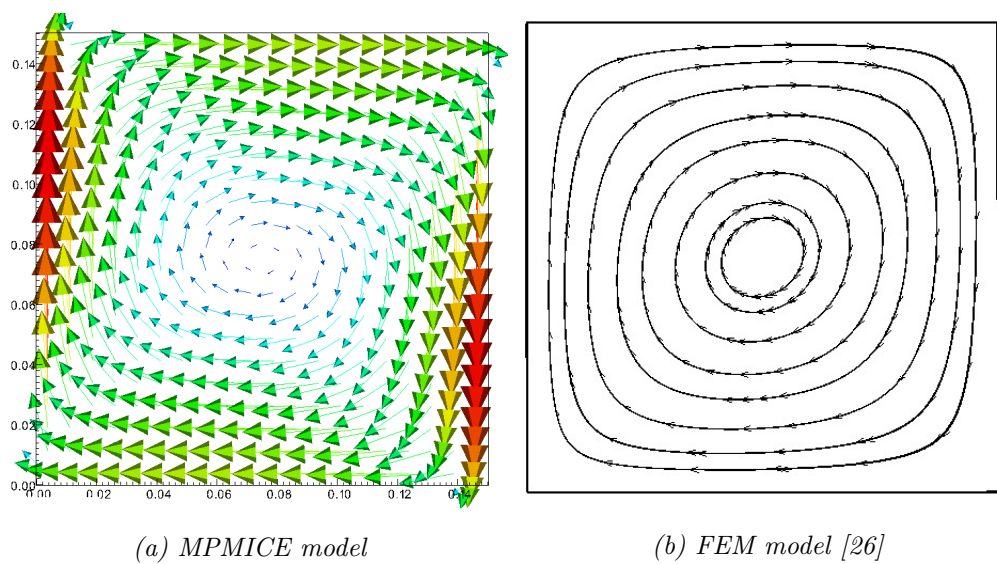
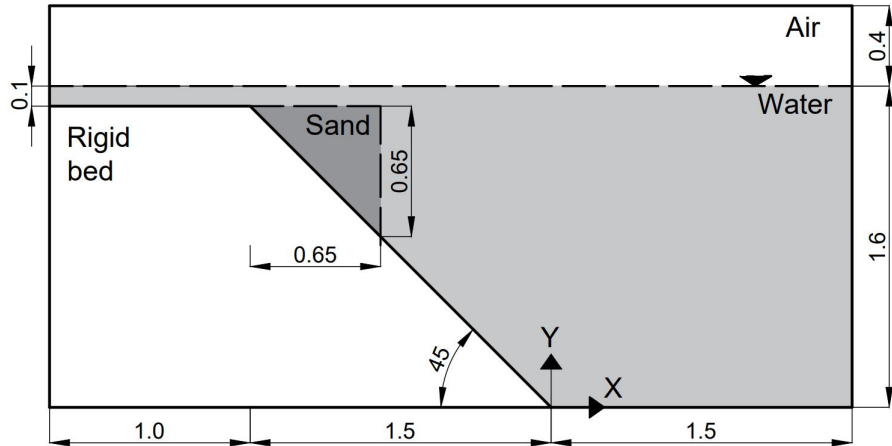


Figure 10: Comparison between MPMICE model and FEM model

521      *Underwater debris flow*



522      *Figure 11: Model schematic*

523      The numerical example is validated using the experimental work of Rzad-  
 524      kiewicz et al. on submarine debris flow [27]. In their experiment, sand within  
 525      a triangular box is released and slides along a rigid bed inclined at 45 degrees  
 526      under water (see Figure 11). The material properties in the numerical model  
 527      are selected based on the experiment by Rzadkiewicz et al. [27]. The sand  
 528      is characterized by a saturated density of  $1985 \text{ kg/m}^3$  and a friction angle  
 529      of 10 degrees. The effect of Young's modulus on debris flow run-out is neg-  
 530      ligible due to the extreme deformation of the debris, so a Young's modulus  
 531      of 50 MPa with a Poisson's ratio of 0.25 is chosen. The rigid bed, being  
 532      much stiffer, has bulk modulus and shear modulus values of  $117E^7 \text{ Pa}$  and  
 533       $43.8E^7 \text{ Pa}$ , respectively. The numerical parameters used in this example are  
 534      presented in Table 1.

535      The boundary conditions imposed in the numerical model are as follows: on  
 536      all boundary faces, the velocity is set to zero ( $U = 0 \text{ m/s}$ ) and the tempera-  
 537      ture is set to 5 degrees Celsius ( $T = 5^\circ\text{C}$ ). At the top boundary, the pressure  
 538      has a Neumann boundary condition of  $d\bar{p}/dx = 0 \text{ kPa}$ , and the density has  
 539      a Neumann boundary condition of  $d\rho/dx = 0 \text{ kg/m}^3$ . The background mesh  
 540      consists of  $700 \times 400$  cells, resulting in a total of 280,000 cells. Each cell in  
 541      the debris flow and rigid bed contains  $2 \times 2$  material points.

542      Figure 13b illustrates snapshots of the underwater debris flow sliding, demon-  
 543      strating that the model captures the typical hydroplaning mechanism of the

543 debris flow. Hydroplaning refers to the lifting of the debris flow, causing it  
 544 to lose contact with the bottom layer. The elevation of the free surface at  
 545 0.4s and 0.8s is compared between our proposed method and other methods  
 546 in Figure 12. Our computed results align well with the experimental results  
 547 [7].

548 Unlike other computational models that rely on total stress analysis [5, 6, 7,  
 549 8], our proposed model utilizes effective stress analysis, enabling the analy-  
 550 sis of water pressure and temperature within the debris flow. Additionally,  
 551 we investigate the differences between underwater debris flow and saturated  
 552 debris flow in terms of their interaction with obstacles. Figure 13 presents  
 553 snapshots of simulations of both underwater and saturated debris flow. The  
 554 saturated debris flow (Figure 13a) exhibits behavior similar to frictional flow,  
 555 where grains have contact forces with each other. Conversely, the underwa-  
 556 ter debris flow (Figure 13b) behaves like turbulent flow, with grains being  
 557 separated from each other and exhibiting no contact forces (as reflected by  
 the near-zero effective stress in the turbulence domain).

Materials	Bulk modul (Pa)	Shear modul (Pa)	Density (kg/m <sup>3</sup> )	Temp (C)	Dynamic viscosity (Pa s)	Friction angle (degrees)
Water (at surface)	2.15e9	-	999.8	5	855e-6	-
Air (at top boundary)	-	-	1.177	5	18.45e-6	-
Sand (porous media)	8.33e6	20e6	1985	5	-	10
Rigid bed (solid)	117e7	43.8e7	8900	5	-	-

Table 1: Numerical parameters for the underwater submarine debris

558

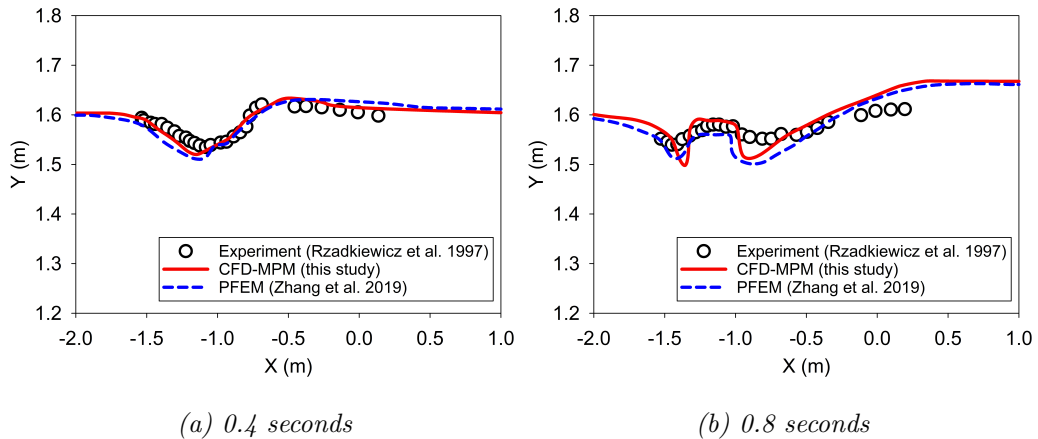


*Figure 12: Evolution of water level in the simulation of underwater debris flow*

559 *Validation of soil response to the seismic loading*

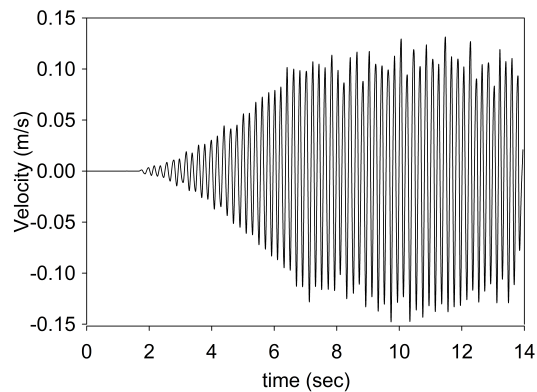


*Figure 14: Seismic loading*

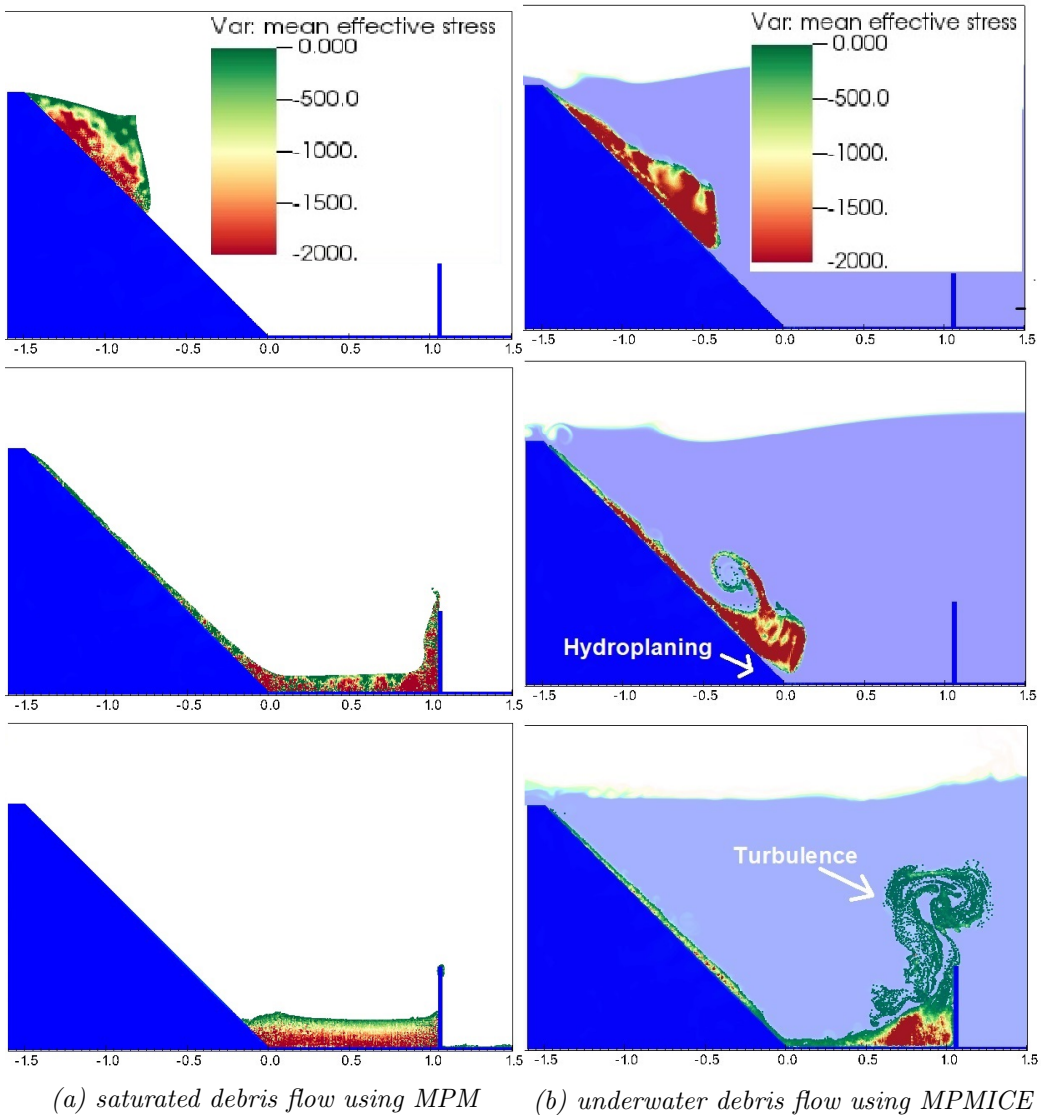
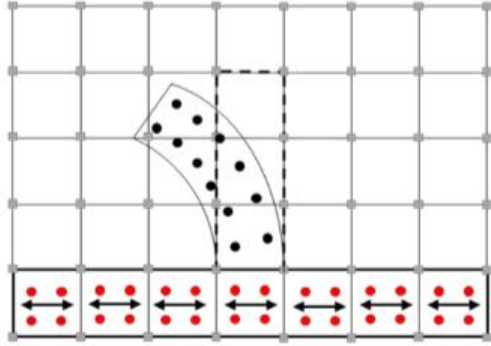
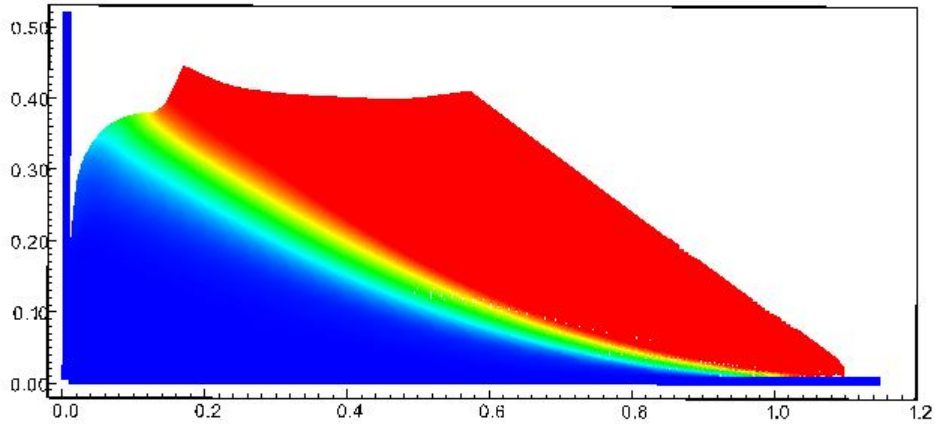


Figure 13: Simulation of Debris Flow: Mean Effective Stress Distribution (Green Color Indicates Near-Zero Effective Stress)



*Figure 15: Material points prescribed velocity as kinematic boundary condition [28]*

560 An experimental study conducted by Hiraoka et al. [29] aimed to invest-  
 561 tigate the influence of seismic shaking on the deformation of a 0.5 m-high  
 562 sand slope. The sand used in the experiment was partially saturated, with a  
 563 moisture content of 10 percent. The provided soil parameters for the Mohr  
 564 Coulomb model include the effective friction angle of 23 degrees, apparent  
 565 cohesion of 0.78 kPa, Young's modulus of 2.57 MPa, and Poisson's ratio of  
 566 0.33, and moist unit weight of 16.5 kN/m<sup>3</sup>. The soil's dilatancy angle was  
 567 assumed to be 0 [29]. The experimental setup consisted of a shaking table  
 568 box with a steel horizontal base and smooth glass vertical sidewalls. Laser  
 569 sensors were used to monitor the displacement of the slope's toe and crest.  
 570 Figure 14 displays the velocity-time history employed in the experiment.



*Figure 16: Numerical model of the seismic-induced slope failure with displacement color*

To simulate the seismic loading in our numerical model, we adopted a method presented by Alsardi et al. [28], which involves specifying the velocity at the corresponding material points representing either the shaking table or the bedrock at the site (see Figure 15). In our simulation, we considered the horizontal base to be fully rough and the vertical contact to be fully smooth. The initial stress condition was initiated using gravity and seismic loading induced the slope failure (see Figure 16). Previous studies by Bhandari et al. [30], Alsardi et al. [28], and Hiraoka et al. [29] attempted to model this experiment using MPM and SPH models. In this study, we compared our results with those obtained from other particle-based methods (Figure 17). The main difference is that we did not apply 5 percent numerical damping in our model, unlike the other methods. We found that the final displacement of the slope toe in our MPM model was higher than that observed in the experiment. Nevertheless, the validation of the Mohr-Coulomb model under seismic response demonstrated a reasonable soil behavior in terms of displacement.

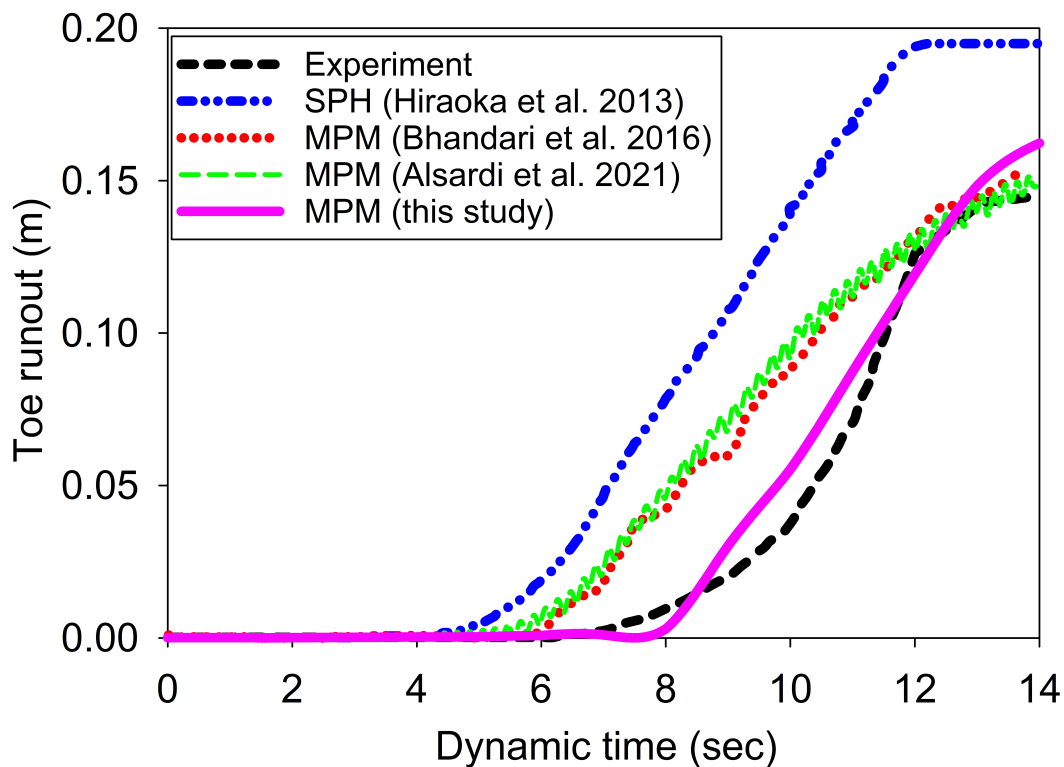


Figure 17: Displacement of the toe of the slope

587 Earthquake-induced submarine landslides

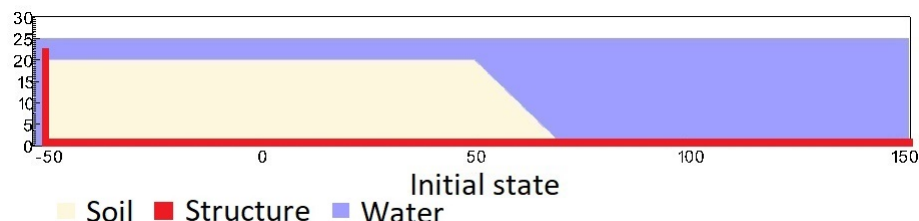
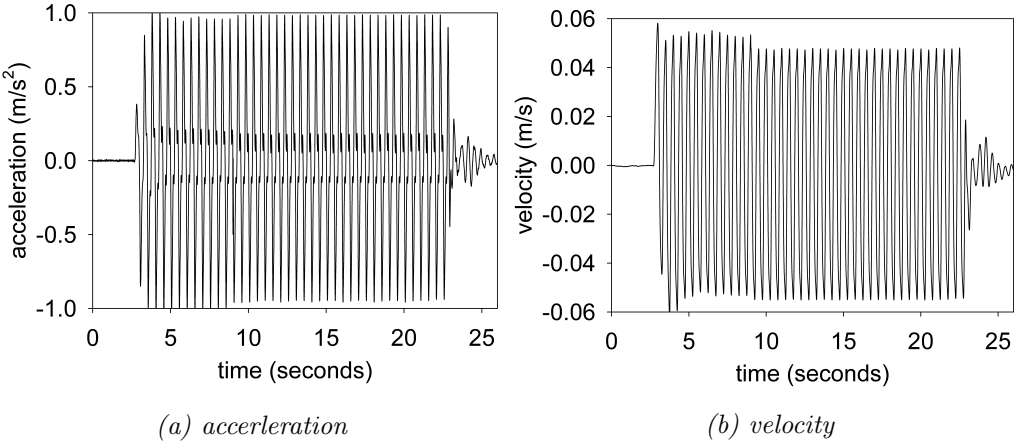


Figure 18: Numerical simulation of the earthquake-induced submarine landslide



*Figure 19: Ground acceleration profile, frequency of 2Hz and magnitude of 1g*

588 In the final example, we perform numerical analysis of the earthquake  
 589 induced submarine landslides. A plane strain model with the slope under  
 590 water is shown in Figure 18. A 20m high slope with slope gradient of 45  
 591 degrees is placed in a horizontal and vertical structure which was used to  
 592 be a scaling table to apply earthquake loading. We simplify the earthquake  
 593 loading by simulating the ground shaking for 20 seconds with the constant  
 594 ground acceleration of 1g and a constant frequency of 2Hz (Figure 19a). The  
 595 ground motion is applied in terms of velocity (Figure 19b). An earthquake  
 596 of this magnitude is possible. For instance, in the case of the 2023 Turkey-  
 597 Syria Earthquake, significant ground shaking with peak ground acceleration  
 598 exceeding 1g was observed at numerous locations. This serves as an example  
 599 of the practical occurrence of such high levels of ground acceleration during  
 600 seismic events. To generate the seismic loading, the same method was used  
 601 as presented in the previous numerical example.

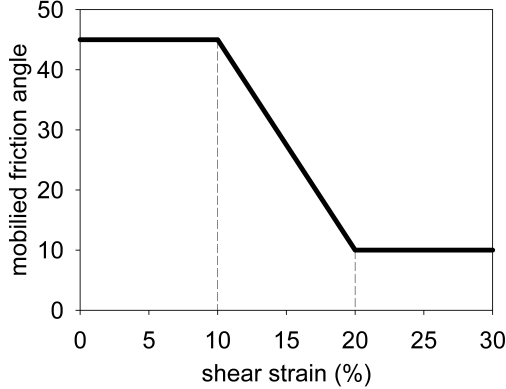
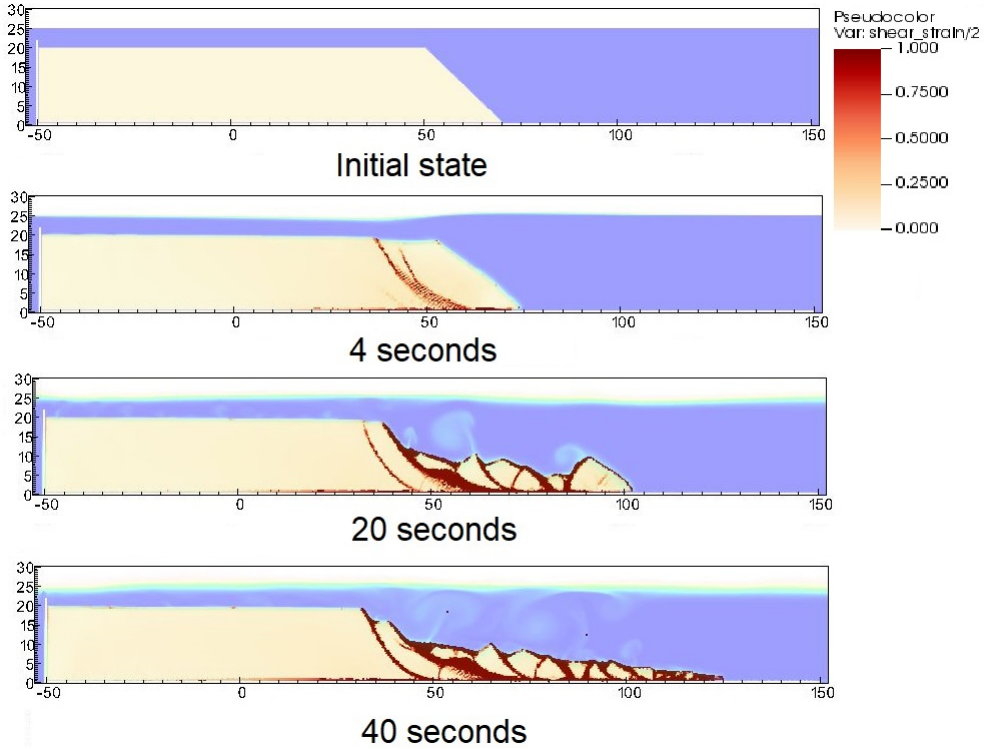


Figure 20: Mobilized friction angle in Mohr Coulomb model

602 A non-associated Mohr-Coulomb model is used for the soil. The soil grain  
 603 has the density of  $2650 \text{ kg/m}^3$ , Young's modulus of 10 kPa and Poisson's  
 604 ratio of 0.3 and zero cohesion. The mobilized friction angle  $\phi'_m$  is governed  
 605 following the softening curve (see Figure 20) with the peak friction angle  $\phi'_p$   
 606 of 45 degrees and the residual friction angle  $\phi'_r$  of 10 degrees. The porosity  
 607 is 0.3 and the average grain size of the soil is around  $0.1 \mu\text{m}$  to mimic the  
 608 undrained behavior. The mobilized dilatancy angle is calculated from the  
 609 Rowe's stress dilatancy theory [31] as follow:

$$\sin \psi'_m = \frac{\sin \phi'_m - \sin \phi'_r}{1 - (\sin \phi'_r \sin \phi'_m)} \quad (100)$$

610 The solid plane is modeled as a rigid body acted as a shaking table. The  
 611 contact between horizontal plane and the sand is the frictional contact with  
 612 the friction coefficient of 0.1. No artificial damping is applied in the simu-  
 613 lation. The contact between vertical plane and the sand is considered to be  
 614 smooth with zero friction coefficient. On all boundary faces, the symmet-  
 615 ric boundary condition is imposed, while the Neumann boundary condition  
 616 is imposed at the top boundary for pressure ( $d\rho/dx = 0 \text{ kPa}$ ) and density  
 617 ( $d\rho/dx = 0 \text{ kg/m}^3$ ). Symmetric boundary condition refers to a condition  
 618 where the normal component of the velocity at the boundary face is set to  
 619 zero, and the tangential component is equal to the tangential component of  
 620 the neighboring cells. The mesh size is  $0.25 \times 0.25 \text{ m}$  with 300852 element  
 621 cells and 142316 material points. The simulation takes a couple of hours to  
 622 perform 60 seconds of the simulation using 4096 CPUs.



*Figure 21: Shear strain during the earthquake-induced submarine landslides*

623 We demonstrate the entire process and the mechanism of the earthquake-  
 624 induced submarine landslides by showing the shear strain (Figure 21), the  
 625 pore water pressure in atm (Figure 22) and the velocity (Figure 23). The  
 626 failure mechanism can be characterized as the progressive failure mechanism.  
 627 Here are some numerical observation:

- 628 1. At the initial of the seismic event, the seismic loading triggers the  
 629 first slide at 3 seconds. At 4 seconds, the debris start to move with the  
 630 maximum speed of around 2-3 m/s with multiple shear band developed  
 631 in the slope. The wave generated from the submarine slide is around  
 632 2-3m towards the slide direction.

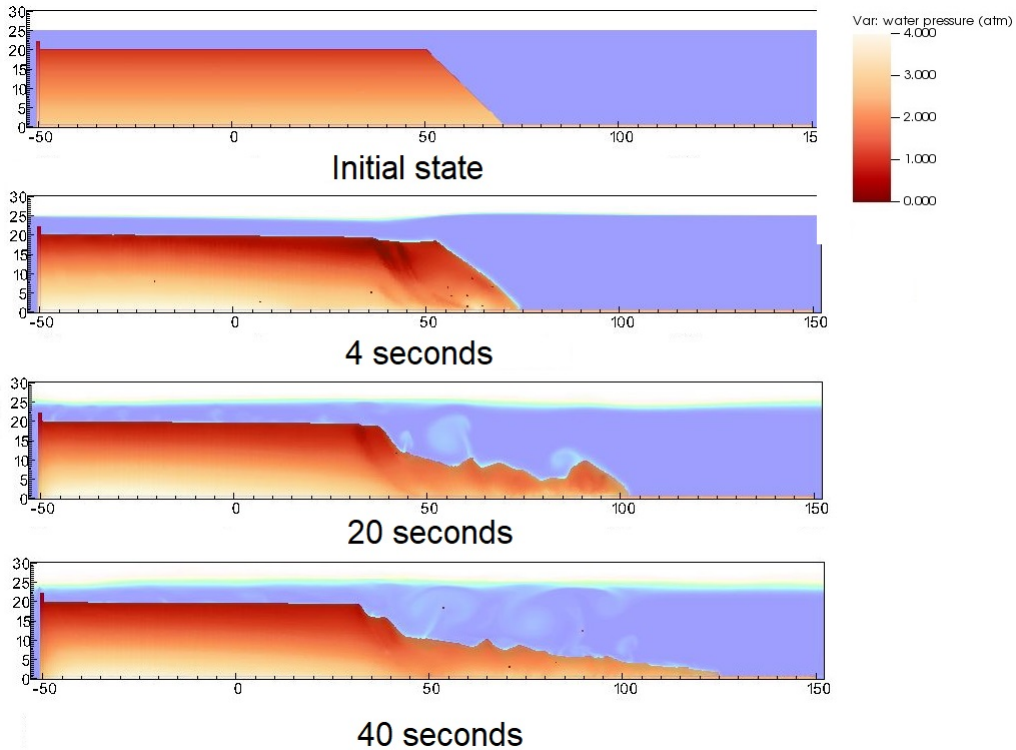


*Figure 22: pore water pressure during the earthquake-induced submarine landslides*

- 633     2. When the onset of the shear band occurs in the slope (for example  
634       at 4 seconds and 20 seconds), the negative excess pore water pressure  
635       is developed along this shear band with pore water pressure is under  
636       1atm. This is a typical dilatancy behavior when the soil is sheared  
637       rapidly in the undrained behavior.
- 638     3. When the seismic loading ends at 23 seconds, the last shear band is  
639       mobilized and the slope soon reaches to the final deposition. No more  
640       progressive failure developed in the slope. The turbulent flow developed  
641       as the interaction between debris flow and seawater.
- 642     Overall, we show the completed process of the earthquake-induced submarine  
643       landslides involving (1) earthquake triggering mechanism, (2) the onset of the  
644       shear band with the development of negative excess pore water pressure, (3)  
645       progressive failure mechanism, (4) submarine landslide induced wave to final  
646       deposition.

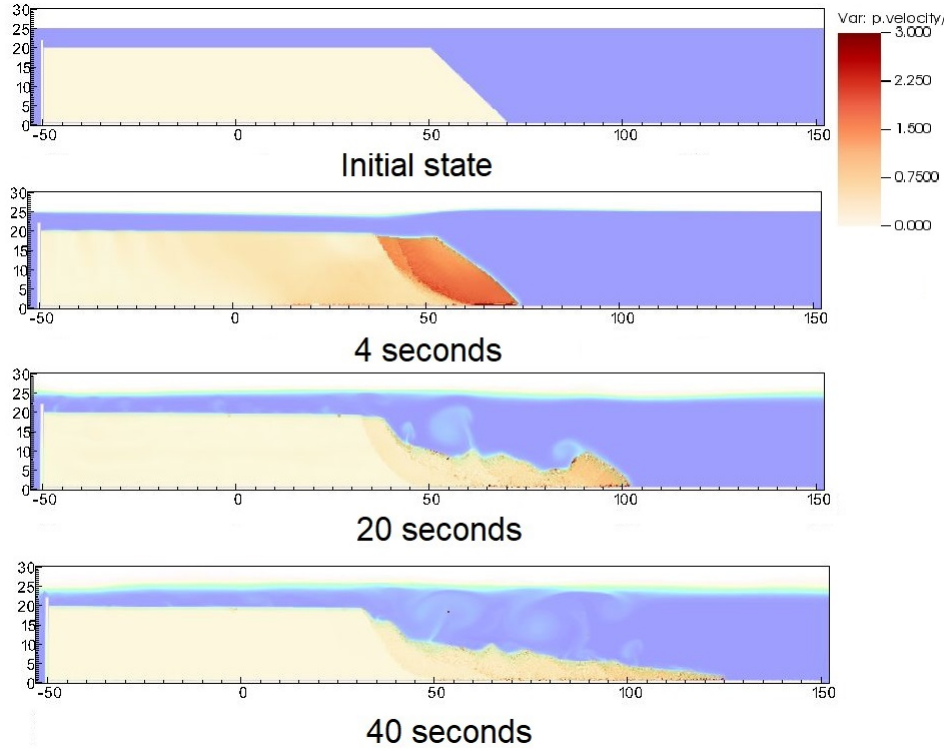


*Figure 23: Velocity during the earthquake-induced submarine landslides*

## 647      **Conclusions**

648      We have presented a numerical approach MPMICE for the simulation  
 649      of large deformation soil-fluid-structure interaction, emphasizing the simu-  
 650      lation of the earthquake-induced submarine landslides. The model uses (1)  
 651      the Material Point Method for capturing the large deformation of iso-thermal  
 652      porous media and solid structures and (2) Implicit Continuous Eulerian (com-  
 653      pressible, conservative multi-material CFD formulation) for modeling the  
 654      complex fluid flow including turbulence. This model is implemented in the  
 655      high-performance Uintah computational framework and validated against an-  
 656      alytical solution and experiment. We then demonstrate the capability of the  
 657      model to simulate the entire process of the earthquake induced submarine  
 658      landslides.

659 **Acknowledgements**

660 The authors gratefully acknowledge Dr. James Guilkey and Dr. Todd  
 661 Harman from the University of Utah for sharing the insight on the theoretical  
 662 framework of MPMICE which this work is based. This project has received  
 663 funding from the European Union's Horizon 2020 research and innovation  
 664 program under the Marie Skłodowska-Curie Actions (MSCA) Individual Fel-  
 665 lowship (Project SUBSLIDE "Submarine landslides and their impacts on  
 666 offshore infrastructures") grant agreement 101022007. The authors would  
 667 also like to acknowledge the support from the Research Council of Norway  
 668 through its Centers of Excellence funding scheme, project number 262644  
 669 Porelab. The computations were performed on High Performance Comput-  
 670 ing resources provided by UNINETT Sigma2 - the National Infrastructure  
 671 for High Performance Computing and Data Storage in Norway.

672 **Appendix: Equation derivation**

673 Before deriving the governing equation, we define the Lagrangian deriva-  
 674 tive for a state variable  $f$  as:

$$\frac{D_f f}{Dt} = \frac{\partial f}{\partial t} + \mathbf{U}_f \cdot \nabla f \quad \frac{D_s f}{Dt} = \frac{\partial f}{\partial t} + \mathbf{U}_s \cdot \nabla f \quad (101)$$

675 we use some definition following [17] as below:

$$-\frac{1}{V} \left[ \frac{\partial V_f}{\partial p} \right] \equiv \kappa_f \quad \text{isothermal compressibility of fluid} \quad (102)$$

$$\frac{1}{V} \left[ \frac{\partial V_f}{\partial T} \right] \equiv \alpha_f \quad \text{constant pressure thermal expansivity of fluid} \quad (103)$$

676 Then, the rate of volume with incompressible solid grains are calculated as  
 677 belows:

$$\frac{1}{V} \frac{D_f V_f}{Dt} = \frac{1}{V} \left( \left[ \frac{\partial V_f}{\partial p} \right] \frac{D_f P_{eq}}{Dt} + \left[ \frac{\partial V_f}{\partial T_f} \right] \frac{D_f T_f}{Dt} \right) = \frac{1}{V} \left( -\kappa_f \frac{D_f P_{eq}}{Dt} + \alpha_f \frac{D_f T_f}{Dt} \right) \quad (104)$$

678 *Evolution of porosity*

679 Solving the solid mass balance equation (4) with the definition of solid  
 680 mass in equation (2), it leads to the rate of porosity as belows:

$$\frac{D_s m_s}{Dt} = \frac{D_s (\phi_s \rho_s V)}{Dt} = \rho_s V \frac{D_s \phi_s}{Dt} + \phi_s V \frac{D_s \rho_s}{Dt} + \phi_s \rho_s \frac{D_s V}{Dt} = 0 \quad (105)$$

681 The soil grains are assumed to be incompressible, therefore, term 2 in the  
 682 right hand side is zero. leading to:

$$V \frac{D_s \phi_s}{Dt} + \phi_s \frac{D_s V}{Dt} = 0 \quad (106)$$

683 Dividing all terms with  $V$  with the equation  $\frac{1}{V} \frac{D_s V}{Dt} = \nabla \cdot \mathbf{U}_s$ , it leads to:

$$\frac{D_s n}{Dt} = \frac{\partial n}{\partial t} + \mathbf{U}_s \cdot \nabla n = \phi_s \nabla \cdot \mathbf{U}_s \quad (107)$$

684 **Momentum conservation**

685 The linear momentum balance equations for the fluid phases based on  
 686 mixture theory are:

$$\frac{1}{V} \frac{D_f(m_f \mathbf{U}_f)}{Dt} = \nabla \cdot (-\phi_f p_f \mathbf{I}) + \nabla \cdot \boldsymbol{\tau}_f + \bar{\rho}_f \mathbf{b} + \sum \mathbf{f}_d + \mathbf{f}_b \quad (108)$$

688 On the right hand sand, the first term is the divergence of partial fluid phase  
 689 stress, the third term is the body force, the fourth term is the drag force  
 690 (momentum exchange) and the fifth term is the buoyant force described in  
 691 [32] for the immiscible mixtures. The buoyant force is in the form as belows:

$$\mathbf{f}_b = \boldsymbol{\sigma}_f \nabla(n) \quad (109)$$

692 As a result, the linear momentum balance equations for the fluid phases  
 693 become as:

$$\frac{1}{V} \frac{D_f(m_f \mathbf{U}_f)}{Dt} = \frac{1}{V} \left[ \frac{\partial(m_f \mathbf{U}_f)}{\partial t} + \nabla \cdot (m_f \mathbf{U}_f \mathbf{U}_f) \right] = -\phi_f \nabla p_f + \nabla \cdot \boldsymbol{\tau}_f + \bar{\rho}_f \mathbf{b} + \sum \mathbf{f}_d \quad (110)$$

694 The Reynolds stress component can be included in the term  $\boldsymbol{\tau}_f$  to consider the  
 695 turbulent effects if needed. To derive the linear momentum balance equation  
 696 for the solid phase, we begin with the linear momentum balance equation for  
 697 the mixture as:

$$\frac{1}{V} \frac{D_f(m_f \mathbf{U}_f)}{Dt} + \frac{1}{V} \frac{D_s(m_s \mathbf{U}_s)}{Dt} = \nabla \cdot (\boldsymbol{\sigma}) + \bar{\rho}_f \mathbf{b} + \bar{\rho}_s \mathbf{b} \quad (111)$$

698 Combining Terzaghi's equation (3) and subtracting both sides with equation  
 699 (110), we obtain the linear momentum balance equations for the solid phase  
 700 as:

$$\frac{1}{V} \frac{D_s(m_s \mathbf{U}_s)}{Dt} = \nabla \cdot (\boldsymbol{\sigma}') - \phi_s \nabla p_f + \bar{\rho}_s \mathbf{b} - \sum \mathbf{f}_d + \sum \mathbf{f}_{fric} \quad (112)$$

701 Here the  $\mathbf{f}_{fric}$  stems from the soil-structure interaction following the contact  
 702 law between the soil/structure interfaces.

703 *Energy conservation*

704 We adopt the general form of the total energy balance equation for the  
 705 porous media from [33], the total energy balance equations for the fluid phases  
 706 are:

$$\frac{1}{V} \frac{D_f(m_f(e_f + 0.5\mathbf{U}_f^2))}{Dt} = \nabla \cdot (-np_f \mathbf{I}) \cdot \mathbf{U}_f + \nabla \cdot \mathbf{q}_f + (\bar{\rho}_f \mathbf{b}) \cdot \mathbf{U}_f + \sum \mathbf{f}_d \cdot \mathbf{U}_f + \sum q_{sf} \quad (113)$$

707 Applying the product rule  $D(m\mathbf{U}^2) = D(m\mathbf{U} \cdot \mathbf{U}) = 2\mathbf{U} \cdot D(m\mathbf{U})$ , the left  
 708 hand side of equation (113) becomes:

$$709 \frac{1}{V} \frac{D_f(m_f(e_f + 0.5\mathbf{U}_f^2))}{Dt} = \frac{1}{V} \frac{D_f(m_f e_f)}{Dt} + \frac{1}{V} \frac{D_f(m_f \mathbf{U}_f)}{Dt} \cdot \mathbf{U}_f \quad (114)$$

710 Combining equations (110), (113), (114), we obtain the final form of the  
 711 internal energy balance equation for the fluid phases as:

$$\frac{1}{V} \frac{D_f(m_f e_f)}{Dt} = \frac{1}{V} \left[ \frac{\partial(m_f e_f)}{\partial t} + \nabla \cdot (m_f e_f \mathbf{U}_f) \right] = \bar{\rho}_f p_f \frac{D_f v_f}{Dt} + \nabla \cdot \mathbf{q}_f + \sum q_{sf} \quad (115)$$

712 On the right hand side, the terms include the average pressure-volume work,  
 713 the average viscous dissipation, the thermal transport and the energy ex-  
 714 change between solid and fluid respectively. The heat flux is  $\mathbf{q}_f = \bar{\rho}_f \beta_f \nabla T_f$   
 715 with  $\beta_f$  being the thermal conductivity coefficient. To derive the internal  
 716 energy balance equation for the solid phase, we introduce the rate of the  
 717 internal energy for the thermoelastic materials as a function of elastic strain  
 718 tensor  $\boldsymbol{\epsilon}_s^e$  and temperature  $T_s$  as belows:

$$\frac{m_s}{V} \frac{D_s(e_s)}{Dt} = \boldsymbol{\sigma}' : \frac{D_s(\boldsymbol{\epsilon}_s^e)}{Dt} + \frac{D_s(e_s)}{D_s(T_s)} \frac{D_s(T_s)}{Dt} = \boldsymbol{\sigma}' : \frac{D_s(\boldsymbol{\epsilon}_s^e)}{Dt} + c_v \frac{D_s(T_s)}{Dt} \quad (116)$$

719  $c_v$  is the specific heat at the constant volume of the solid materials. The total  
 720 energy balance equation for the mixture based on [33] can be written as:

$$721 \frac{1}{V} \frac{D_f(m_f(e_f + 0.5\mathbf{U}_f^2))}{Dt} + \frac{1}{V} \frac{D_s(m_s(e_s + 0.5\mathbf{U}_s^2))}{Dt} = \nabla \cdot (-\phi_f p_f \mathbf{I}) \cdot \mathbf{U}_f \\ + \nabla \cdot (\boldsymbol{\sigma}' - \phi_s p_f \mathbf{I}) \cdot \mathbf{U}_s + (-\phi_f p_f \mathbf{I}) : \nabla \mathbf{U}_f + \boldsymbol{\sigma}' : \nabla \mathbf{U}_s \\ + (\bar{\rho}_f \mathbf{b}) \cdot \mathbf{U}_f + (\bar{\rho}_s \mathbf{b}) \cdot \mathbf{U}_s + \nabla \cdot \mathbf{q}_f + \nabla \cdot \mathbf{q}_s + \sum \mathbf{f}_d \cdot (\mathbf{U}_f - \mathbf{U}_s) \quad (117)$$

722 Subtracting equation (117), (116) to equations (113) and (112), we obtained  
 723 the internal energy balance equation for solid phase as:

$$\boldsymbol{\sigma}' : \frac{D_s(\epsilon_s^e)}{Dt} + \frac{m_s}{V} c_v \frac{D_s(T_s)}{Dt} = \Delta W_s + \Delta W_{friction} + \nabla \cdot \mathbf{q}_s - \sum q_{sf} \quad (118)$$

724 On the right hand side, the terms include the work rate from frictional sliding  
 725 between solid materials  $\Delta W_{friction}$ , thermal transport and energy exchange  
 726 between solid and fluid respectively. The heat flux is  $\mathbf{q}_s = \bar{\rho}_s \beta_s \nabla T_s$  with  $\beta_s$   
 727 being the thermal conductivity of the solid materials, the mechanical work  
 728 rate  $\Delta W_s = \boldsymbol{\sigma}' : \frac{D_s(\epsilon_s^e)}{Dt} = \boldsymbol{\sigma}' : (\frac{D_s(\epsilon_s^e)}{Dt} + \frac{D_s(\epsilon_s^p)}{Dt})$  computed from the constitutive  
 729 model with  $\epsilon_s^p$  is the plastic strain tensor, . By subtracting the term  $\boldsymbol{\sigma}' : \frac{D_s(\epsilon_s^e)}{Dt}$ ,  
 730 we get the final form of the energy balance equation as:

$$\frac{m_s}{V} c_v \frac{D_s(T_s)}{Dt} = \boldsymbol{\sigma}' : \frac{D_s(\epsilon_s^p)}{Dt} + \Delta W_{friction} + \nabla \cdot \mathbf{q}_s - \sum q_{sf} \quad (119)$$

### 731 Advanced Fluid Pressure

732 The discretization of the pressure equation begins with the Lagrangian  
 733 cell face velocity and the equation for the pressure as:

$$\bar{\rho}_{f,FC} \frac{\mathbf{U}_{f,FC}^{n+1} - \mathbf{U}_{f,FC}^n}{dt} = n \nabla^{FC} P_{f,c}^{n+1} + \bar{\rho}_{f,FC} \mathbf{b} \quad (120)$$

734

$$\kappa \frac{dP}{dt} = \nabla^c \cdot \mathbf{U}_{f,FC}^{n+1} \quad (121)$$

735 The divergence of the equation (120) with  $\nabla \cdot \mathbf{b} = 0$  is:

$$\nabla^c \cdot \mathbf{U}_{f,FC}^{n+1} - \nabla^c \cdot \mathbf{U}_{f,FC}^n = \nabla^c \frac{\Delta t}{\rho_{f,FC}^n} \cdot \nabla^{FC} (P_{f,c}^n + \Delta P_{f,c}^n) \quad (122)$$

736 To solve this equation, we define the cell face intermediate velocity  $\mathbf{U}_{f,FC}^*$  as:

$$\bar{\rho}_{f,FC} \frac{\mathbf{U}_{f,FC}^* - \mathbf{U}_{f,FC}^n}{\Delta t} = n \nabla^{FC} P_{f,c}^n + \bar{\rho}_{f,FC} \mathbf{b} \quad (123)$$

737 The divergence of the equation (123) is:

$$\nabla^c \cdot \mathbf{U}_{f,FC}^* - \nabla^c \cdot \mathbf{U}_{f,FC}^n = \nabla^c \frac{\Delta t}{\rho_{f,FC}^n} \cdot \nabla^{FC} P_{f,c}^n \quad (124)$$

<sup>738</sup> Combining equations (121, 122, 124), it leads to:

$$\left( \kappa - \nabla^c \frac{\Delta t}{\rho_{f,FC}^n} \cdot \nabla^{FC} \right) \Delta P_{fc}^n = -\nabla^c \cdot \mathbf{U}_{f,FC}^* \quad (125)$$

<sup>739</sup> When the fluid is incompressible,  $\kappa$  approaches to zero and the equation  
<sup>740</sup> (125) becomes the Poisson's equation for the incompressible fluid flow.

<sup>741</sup> *Momentum and Energy exchange with an implicit solver*

<sup>742</sup> Considering the fluid momentum balance equation as:

$$(m\mathbf{U})_{f,FC}^{n+1} = (m\mathbf{U})_{f,FC}^n - \Delta t(Vn\nabla^{FC}P_{f,c}^n + m_f\mathbf{b}) + VK\Delta t(\mathbf{U}_{s,FC}^{n+1} - \mathbf{U}_{f,FC}^{n+1}) \quad (126)$$

<sup>743</sup> And assuming  $m_{f,FC}^{n+1} = m_{f,FC}^n$ , we get:

$$\mathbf{U}_{f,FC}^{n+1} = \mathbf{U}_{f,FC}^n - \Delta t\left(\frac{\nabla^{FC}P_{fc}^n}{\rho_{f,FC}^n} + \mathbf{b}\right) + \frac{\Delta tK}{\bar{\rho}_{f,FC}^n}(\mathbf{U}_{s,FC}^{n+1} - \mathbf{U}_{f,FC}^{n+1}) \quad (127)$$

<sup>744</sup> As defined in the section 'Advanced Fluid Pressure', the cell face intermediate  
<sup>745</sup> fluid velocity  $\mathbf{U}_{f,FC}^* = \Delta t(\nabla^{FC}P_{fc}^n/\rho_{f,FC}^n + \mathbf{b})$  is computed as:

$$\mathbf{U}_{f,FC}^{n+1} = \mathbf{U}_{f,FC}^* + \frac{\Delta tK}{\bar{\rho}_{f,FC}^n}(\mathbf{U}_{s,FC}^{n+1} - \mathbf{U}_{f,FC}^{n+1}) \quad (128)$$

<sup>746</sup> Considering the solid momentum balance equation as:

$$(m\mathbf{U})_{s,FC}^{n+1} = (m\mathbf{U})_{s,FC}^n - \Delta t(V\nabla^{FC} \cdot \boldsymbol{\sigma}'^n - V(1-n)\nabla^{FC}P_{f,c}^n + m_s\mathbf{b}) - VK\Delta t(\mathbf{U}_{s,FC}^{n+1} - \mathbf{U}_{f,FC}^{n+1}) \quad (129)$$

<sup>747</sup> We define the cell face intermediate solid velocity as  $\mathbf{U}_{s,FC}^* = \Delta t(\nabla^{FC} \cdot \boldsymbol{\sigma}'^n / \bar{\rho}_{s,FC}^n - \nabla^{FC}P_{f,c}^n / \rho_s + \mathbf{b})$  leading to:

$$\mathbf{U}_{s,FC}^{n+1} = \mathbf{U}_{s,FC}^* - \frac{\Delta tK}{\bar{\rho}_{s,FC}^n}(\mathbf{U}_{s,FC}^{n+1} - \mathbf{U}_{f,FC}^{n+1}) \quad (130)$$

<sup>749</sup> Combining equation (128) and (130) we get:

$$\begin{aligned} \mathbf{U}_{f,FC}^* + \Delta\mathbf{U}_{f,FC} &= \mathbf{U}_{f,FC}^* + \frac{\Delta tK}{\bar{\rho}_{f,FC}^n}(\mathbf{U}_{s,FC}^* + \Delta\mathbf{U}_{s,FC} - \mathbf{U}_{f,FC}^* - \Delta\mathbf{U}_{f,FC}) \\ \mathbf{U}_{s,FC}^* + \Delta\mathbf{U}_{s,FC} &= \mathbf{U}_{s,FC}^* - \frac{\Delta tK}{\bar{\rho}_{s,FC}^n}(\mathbf{U}_{s,FC}^* + \Delta\mathbf{U}_{s,FC} - \mathbf{U}_{f,FC}^* - \Delta\mathbf{U}_{f,FC}) \end{aligned} \quad (131)$$

750 Rearranging the equation (131), it leads to the linear system of equations as  
 751 belows:

$$\begin{vmatrix} (1 + \beta_{12,FC}) & -\beta_{12,FC} \\ -\beta_{21,FC} & (1 + \beta_{21,FC}) \end{vmatrix} \begin{vmatrix} \Delta \mathbf{U}_{f,FC} \\ \Delta \mathbf{U}_{s,FC} \end{vmatrix} = \begin{vmatrix} \beta_{12,FC}(\mathbf{U}_{s,FC}^* - \mathbf{U}_{f,FC}^*) \\ \beta_{21,FC}(\mathbf{U}_{f,FC}^* - \mathbf{U}_{s,FC}^*) \end{vmatrix}$$

752 Solving this linear equations with  $\beta_{12,FC} = (\Delta t K) / \bar{\rho}_{f,FC}^n$  and  $\beta_{21,FC} =$   
 753  $(\Delta t K) / \bar{\rho}_{s,FC}^n$  with K is the momentum exchange coefficient. Similar deriva-  
 754 tion can be performed to computed the cell-center velocity increment leading  
 755 to:

$$\begin{vmatrix} (1 + \beta_{12c}) & -\beta_{12c} \\ -\beta_{21c} & (1 + \beta_{21c}) \end{vmatrix} \begin{vmatrix} \Delta \mathbf{U}_{f,c} \\ \Delta \mathbf{U}_{sc} \end{vmatrix} = \begin{vmatrix} \beta_{12c}(\mathbf{U}_{sc}^* - \mathbf{U}_{f,c}^*) \\ \beta_{21c}(\mathbf{U}_{f,c}^* - \mathbf{U}_{sc}^*) \end{vmatrix}$$

756 with  $\beta_{12c} = (\Delta t K) / \bar{\rho}_{f,c}^n$  and  $\beta_{21c} = (\Delta t K) / \bar{\rho}_{sc}^n$  and the cell-centered interme-  
 757 diate velocity can be calculated by:

$$\begin{aligned} \mathbf{U}_{f,c}^* &= \mathbf{U}_{f,c}^n + \Delta t \left( -\frac{\nabla P_{f,c}^{n+1}}{\rho_{f,c}^n} + \frac{\nabla \cdot \boldsymbol{\tau}_{f,c}^n}{\bar{\rho}_{f,c}^n} + \mathbf{b} \right) \\ \mathbf{U}_{sc}^* &= \mathbf{U}_{sc}^n + \Delta t \left( \frac{\nabla \cdot \boldsymbol{\sigma}_c'^n}{\bar{\rho}_{sc}^n} - \frac{\nabla P_{f,c}^{n+1}}{\rho_s} + \mathbf{b} \right) \end{aligned} \quad (132)$$

758 For generalize multi materials i,j = 1:N, the linear equations is in the form  
 759 as:

$$\begin{vmatrix} (1 + \beta_{ij}) & -\beta_{ij} \\ -\beta_{ji} & (1 + \beta_{ji}) \end{vmatrix} \begin{vmatrix} \Delta \mathbf{U}_i \\ \Delta \mathbf{U}_j \end{vmatrix} = \begin{vmatrix} \beta_{ij}(\mathbf{U}_i^* - \mathbf{U}_j^*) \\ \beta_{ji}(\mathbf{U}_j^* - \mathbf{U}_i^*) \end{vmatrix}$$

760 Similar approach applied for the ernergy exchange term leading to:

$$\begin{vmatrix} (1 + \eta_{ij}) & -\eta_{ij} \\ -\eta_{ji} & (1 + \eta_{ji}) \end{vmatrix} \begin{vmatrix} \Delta T_i \\ \Delta T_j \end{vmatrix} = \begin{vmatrix} \eta_{ij}(T_i^n - T_j^n) \\ \eta_{ji}(T_j^n - T_i^n) \end{vmatrix}$$

761 with  $\eta$  is the energy exchange coefficient.

## 762 References

- 763 [1] D. Yuk, S. Yim, P.-F. Liu, Numerical modeling of submarine mass-  
 764 movement generated waves using RANS model, Computers and Geo-  
 765 sciences 32 (7) (2006) 927–935. doi:10.1016/j.cageo.2005.10.028.  
 766 URL <https://doi.org/10.1016/j.cageo.2005.10.028>

- 767 [2] S. Glimsdal, J.-S. L'Heureux, C. B. Harbitz, F. Løvholt, The 29th january 2014 submarine landslide at statland, norway—landslide dynamics,  
768 tsunami generation, and run-up, *Landslides* 13 (6) (2016) 1435–1444.  
769 doi:10.1007/s10346-016-0758-7.  
770 URL <https://doi.org/10.1007/s10346-016-0758-7>
- 772 [3] S. Abadie, D. Morichon, S. Grilli, S. Glockner, Numerical simulation  
773 of waves generated by landslides using a multiple-fluid navier–stokes model,  
774 *Coastal Engineering* 57 (9) (2010) 779–794.  
775 doi:10.1016/j.coastaleng.2010.03.003.  
776 URL <https://doi.org/10.1016/j.coastaleng.2010.03.003>
- 777 [4] M. Rauter, S. Viroulet, S. S. Gylfadóttir, W. Fellin, F. Løvholt, Granular  
778 porous landslide tsunami modelling – the 2014 lake askja flank collapse,  
779 *Nature Communications* 13 (1) (Feb. 2022). doi:10.1038/s41467-022-  
780 28296-7.  
781 URL <https://doi.org/10.1038/s41467-022-28296-7>
- 782 [5] Q.-A. Tran, W. Sołowski, Generalized interpolation material point  
783 method modelling of large deformation problems including strain-  
784 rate effects – application to penetration and progressive failure  
785 problems, *Computers and Geotechnics* 106 (2019) 249–265.  
786 doi:10.1016/j.compgeo.2018.10.020.  
787 URL <https://doi.org/10.1016/j.compgeo.2018.10.020>
- 788 [6] T. Capone, A. Panizzo, J. J. Monaghan, SPH modelling of water  
789 waves generated by submarine landslides, *Journal of Hydraulic Research*  
790 48 (sup1) (2010) 80–84. doi:10.1080/00221686.2010.9641248.  
791 URL <https://doi.org/10.1080/00221686.2010.9641248>
- 792 [7] X. Zhang, E. Oñate, S. A. G. Torres, J. Bleyer, K. Krabbenhoft, A  
793 unified lagrangian formulation for solid and fluid dynamics and its possi-  
794 bility for modelling submarine landslides and their consequences, *Computer  
795 Methods in Applied Mechanics and Engineering* 343 (2019) 314–  
796 338. doi:10.1016/j.cma.2018.07.043.  
797 URL <https://doi.org/10.1016/j.cma.2018.07.043>
- 798 [8] R. Dey, B. C. Hawlader, R. Phillips, K. Soga, Numerical modelling  
799 of submarine landslides with sensitive clay layers, *Géotechnique* 66 (6)

- 800        (2016) 454–468. doi:10.1680/jgeot.15.p.111.  
801        URL <https://doi.org/10.1680/jgeot.15.p.111>
- 802 [9] S. Bandara, K. Soga, Coupling of soil deformation and pore fluid flow  
803        using material point method, *Computers and Geotechnics* 63 (2015)  
804        199–214. doi:10.1016/j.compgeo.2014.09.009.  
805        URL <https://doi.org/10.1016/j.compgeo.2014.09.009>
- 806 [10] A. P. Tampubolon, T. Gast, G. Klár, C. Fu, J. Teran, C. Jiang,  
807        K. Museth, Multi-species simulation of porous sand and water  
808        mixtures, *ACM Transactions on Graphics* 36 (4) (2017) 1–11.  
809        doi:10.1145/3072959.3073651.  
810        URL <https://doi.org/10.1145/3072959.3073651>
- 811 [11] A. S. Baumgarten, K. Kamrin, A general constitutive model for dense,  
812        fine-particle suspensions validated in many geometries, *Proceedings*  
813        of the National Academy of Sciences
- 814        116 (42) (2019) 20828–20836.  
815        doi:10.1073/pnas.1908065116.  
816        URL <https://doi.org/10.1073/pnas.1908065116>
- 817 [12] Q.-A. Tran, W. Sołowski, Temporal and null-space filter for the  
818        material point method, *International Journal for Numerical Methods in  
819        Engineering* 120 (3) (2019) 328–360. doi:10.1002/nme.6138.  
820        URL <https://doi.org/10.1002/nme.6138>
- 821 [13] X. Zheng, F. Pisanò, P. J. Vardon, M. A. Hicks, An explicit stabilised  
822        material point method for coupled hydromechanical problems in two-  
823        phase porous media, *Computers and Geotechnics* 135 (2021) 104112.  
824        doi:10.1016/j.compgeo.2021.104112.  
825        URL <https://doi.org/10.1016/j.compgeo.2021.104112>
- 826 [14] Q. A. Tran, W. Sołowski, M. Berzins, J. Guilkey, A convected particle  
827        least square interpolation material point method, *International Journal  
828        for Numerical Methods in Engineering* 121 (6) (2019) 1068–1100.  
829        doi:10.1002/nme.6257.  
830        URL <https://doi.org/10.1002/nme.6257>
- 831 [15] J.-S. Chen, M. Hillman, S.-W. Chi, Meshfree methods: Progress made  
832        after 20 years, *Journal of Engineering Mechanics* 143 (4) (Apr. 2017).

- 832 doi:10.1061/(asce)em.1943-7889.0001176.  
833 URL [https://doi.org/10.1061/\(asce\)em.1943-7889.0001176](https://doi.org/10.1061/(asce)em.1943-7889.0001176)
- 834 [16] F. H. Harlow, A. A. Amsden, Numerical calculation of almost incom-  
835 pressible flow, *Journal of Computational Physics* 3 (1) (1968) 80–93.  
836 doi:[https://doi.org/10.1016/0021-9991\(68\)90007-7](https://doi.org/10.1016/0021-9991(68)90007-7).  
837 URL <https://www.sciencedirect.com/science/article/pii/0021999168900077>
- 838 [17] B. A. Kashiwa, A multifield model and method for fluid-structure in-  
839 teraction dynamics, *Tech. Rep. LA-UR-01-1136*, Los Alamos National  
840 Laboratory (2001).
- 841 [18] J. Guilkey, T. Harman, B. Banerjee, An eulerian-lagrangian  
842 approach for simulating explosions of energetic devices,  
843 *Computers and Structures* 85 (11) (2007) 660 – 674.  
844 doi:<https://doi.org/10.1016/j.compstruc.2007.01.031>.  
845 URL <http://www.sciencedirect.com/science/article/pii/S0045794907000429>
- 846 [19] A. S. Baumgarten, B. L. Couchman, K. Kamrin, A coupled finite volume  
847 and material point method for two-phase simulation of liquid-sediment  
848 and gas-sediment flows, *Computer Methods in Applied Mechanics and*  
849 *Engineering* 384 (2021) 113940. doi:10.1016/j.cma.2021.113940.  
850 URL <https://doi.org/10.1016/j.cma.2021.113940>
- 851 [20] J. Clausen, L. Damkilde, L. Andersen, Efficient return algorithms for  
852 associated plasticity with multiple yield planes, *International Journal*  
853 *for Numerical Methods in Engineering* 66 (6) (2006) 1036–1059.  
854 arXiv:<https://onlinelibrary.wiley.com/doi/pdf/10.1002/nme.1595>,  
855 doi:<https://doi.org/10.1002/nme.1595>.  
856 URL <https://onlinelibrary.wiley.com/doi/abs/10.1002/nme.1595>
- 857 [21] P. Moin, K. Squires, W. Cabot, S. Lee, A dynamic  
858 subgrid-scale model for compressible turbulence and scalar  
859 transport, *Physics of Fluids A: Fluid Dynamics* 3 (11)  
860 (1991) 2746–2757. arXiv:[https://pubs.aip.org/aip/pof/article-pdf/3/11/2746/12328150/2746\\_1\\_online.pdf](https://pubs.aip.org/aip/pof/article-pdf/3/11/2746/12328150/2746_1_online.pdf), doi:10.1063/1.858164.  
861 URL <https://doi.org/10.1063/1.858164>
- 863 [22] S. Bardenhagen, J. Guilkey, K. Roessig, J. Brackbill, W. Witzel,  
864 J.C.Foster, An improved contact algorithm for the material point

- method and application to stress propagation in granular material, CMES-Computer Modeling in Engineering and Sciences 2 (2001) 509–522. doi:10.3970/cmes.2001.002.509.
- [23] J. A. M. K. R. Beetstra, M. A. van der Hoef, Drag force of intermediate reynolds number flow past mono- and bidisperse arrays of spheres, Fluid Mechanics and Transport Phenomena 53 (2) (2007) 489 – 501. doi:<https://doi.org/10.1002/aic.11065>.
- [24] R. W. Stewart, The air-sea momentum exchange, Boundary-Layer Meteorology 6 (1-2) (1974) 151–167. doi:10.1007/bf00232481.  
URL <https://doi.org/10.1007/bf00232481>
- [25] S. G. Bardenhagen, E. M. Kober, The generalized interpolation material point method, Computer Modeling in Engineering and Sciences 5 (2004) 477–496. doi:10.1016/j.compgeo.2004.005.477  
URL <https://doi.org/10.3970/cmes.2004.005.477>
- [26] S. G. Amiri, E. Taheri, A. Lavasan, A hybrid finite element model for non-isothermal two-phase flow in deformable porous media, Computers and Geotechnics 135 (2021) 104199. doi:10.1016/j.compgeo.2021.104199.  
URL <https://doi.org/10.1016/j.compgeo.2021.104199>
- [27] S. A. R. C. Mariotti, P. Heinrich, Numerical simulation of submarine landslides and their hydraulic effects, Journal of Waterway, Port, Coastal, and Ocean Engineering 123 (4) (1997). doi:[https://doi.org/10.1061/\(ASCE\)0733-950X\(1997\)123:4\(149\)](https://doi.org/10.1061/(ASCE)0733-950X(1997)123:4(149)).
- [28] A. Alsardi, A. Yerro, Runout Modeling of Earthquake-Triggered Landslides with the Material Point Method, pp. 21–31. arXiv:<https://ascelibrary.org/doi/pdf/10.1061/9780784483428.003>, doi:10.1061/9780784483428.003.  
URL <https://ascelibrary.org/doi/abs/10.1061/9780784483428.003>
- [29] H. N., O. A., B. H. H., R. P., R. Fukagawa, Seismic slope failuremodelling using the mesh-free sph method, International Journal of Geomate (2013) 660–665.
- [30] T. Bhandari, F. Hamad, C. Moormann, K. Sharma, B. Westrich, Numerical modelling of seismic slope failure using mpm, Computers and Geotechnics 75 (2016) 126–134.

- 898 doi:<https://doi.org/10.1016/j.compgeo.2016.01.017>.  
899 URL <https://www.sciencedirect.com/science/article/pii/S0266352X16000264>
- 900 [31] D. Muir Wood, Soil behaviour and critical state soil mechanics, Cam-  
901 bridge University Press, United Kingdom, 1990.
- 902 [32] D. Drumheller, On theories for reacting immiscible mixtures, Inter-  
903 national Journal of Engineering Science 38 (3) (2000) 347 – 382.  
904 doi:[https://doi.org/10.1016/S0020-7225\(99\)00047-6](https://doi.org/10.1016/S0020-7225(99)00047-6).  
905 URL <http://www.sciencedirect.com/science/article/pii/S0020722599000476>
- 906 [33] S. Hassanzadeh, Derivation of basic equations of mass transport in  
907 porous media, part1: Macroscopic balance laws, Advances in Wa-  
908 ter Resources 9 (1986) 196–206. doi:[https://doi.org/10.1016/0309-1708\(86\)90024-2](https://doi.org/10.1016/0309-1708(86)90024-2).
- 909